

Speckle decorrelation in fundamental and second-harmonic light scattered from nonlinear disorder

Rabisankar Samanta,¹ Romain Pierrat,^{2,*} Rémi Carminati,^{2,3} and Sushil Mujumdar^{1,†}

¹*Nano-optics and Mesoscopic Optics Laboratory, Tata Institute of
Fundamental Research, 1 Homi Bhabha Road, Mumbai, 400 005, India*

²*Institut Langevin, ESPCI Paris, PSL University, CNRS, 1 rue Jussieu, 75005 Paris, France*

³*Institut d'Optique Graduate School, Université Paris-Saclay, F-91127 Palaiseau, France*

(Dated: August 4, 2022)

Speckle patterns generated in a disordered medium carry a lot of information despite the apparent complete randomness in the intensity pattern. When the medium possesses $\chi^{(2)}$ nonlinearity, the speckle is sensitive to the phase of the incident fundamental light, as well as the light generated within. Here, we examine the speckle decorrelation in the fundamental and second-harmonic transmitted light as a function of varying power in the fundamental beam. At low incident powers, the speckle patterns produced by successive pulses exhibit strong correlations, that decrease with increasing power. The average correlation in the second-harmonic speckle decays faster than in the fundamental speckle. Next, we construct a theoretical model, backed up by numerical computations, to obtain deeper physical insights on the faster decorrelations in the second-harmonic light. Whilst providing excellent qualitative agreement with the experiments, the model sheds important light on the contribution of two effects in the correlations, namely, the generation of second-harmonic light, and the propagation thereof.

Wave transport in a random medium is a universal phenomenon that transcends the boundaries of various sub-topics such as optics, condensed matter physics, acoustics, or quantum matter etc [1]. Among all of these, transport of optical waves has attracted most attention due to the sophisticated experimental capabilities offered by optics. Indeed, the study of photon transport through disordered media has revealed important facets of transport in all regimes of disorder, from weak scattering occurring in media like fog to strong scattering in dense powders. With increasing disorder, incident waves experience multiple scattering where the transport of intensity is described as a diffusion process. Further increase in disorder leads to exotic phenomena such as weak localization and strong localization are manifest in the system, which essentially represent reduced or arrested photon transport [2]. Traditionally, all these phenomena were studied in the linear regime due to the inherent non-interacting nature of photons. However, interactions can be created by introducing nonlinearities into the media. Materials that respond to higher powers of incident electric fields can be exploited to create disordered systems that favour nonlinear propagation. The consequences of nonlinearity on the physics of light transport in disorder have been extensively addressed both in $\chi^{(3)}$ media, that are media exhibiting intensity-dependent refractive index [3–6], and in $\chi^{(2)}$ media, that can generate second-harmonic frequencies of light [7–13]. In the latter scenario, research efforts have been focused on fundamental physics of diffusion and weak localization in $\chi^{(2)}$ disorder [7–10], and on the applicability of disorder in enhancing nonlinear generation [11–13].

One of the most fundamental effects in disorder that depends on the phase of the propagating light is the appearance of speckle. A speckle pattern is the random intensity distribution of bright and dark spots developed due to the interference of many coherent wavelets with the same frequency and different amplitudes and phases travelling in a disordered medium [14]. Despite the apparent complete randomness in the intensity distribution, various correlations [15] are known to exist in the speckle pattern. For instance, the optical memory effect ‘remembers’ the incoming wavefront under slight perturbation in position and angle [16–20], an idea that has emerged as an efficient tool in imaging through opaque media [21, 22]. Recent theory and experiments have unveiled non-Gaussian and long-range correlations between transmitted and reflected speckle patterns [23–25]. Not surprisingly, the rich physics of speckle correlations has already motivated research in nonlinear systems. For instance, a nonlinear optical memory effect [26] was revealed in a $\chi^{(3)}$ medium, namely a silica aerogel, through a series of pump and probe experiments wherein disordered medium is agitated by an optothermal nonlinearity. Another well-known consequence of $\chi^{(3)}$ nonlinearity is the speckle instability, wherein the speckle pattern fluctuates and becomes unstable when the nonlinearity surpasses a threshold value [27–29]. In the weak localization regime, the speckle patterns formed by nonlinear point scatterers exhibit a dynamic instability and lead to chaotic behavior of the system [30]. Such speckle instabilities in $\chi^{(3)}$ nonlinear disordered media have been experimentally reported [31]. On the other hand, $\chi^{(2)}$ nonlinearity has been employed to primarily investigate angular correlations in speckles. For example, experiments and calculations have shown that angular correlations in reflected speckle scale with sample thickness for second-harmonic light, in contrast to scaling with mean

* romain.pierrat@espci.psl.eu

† mujumdar@tifr.res.in

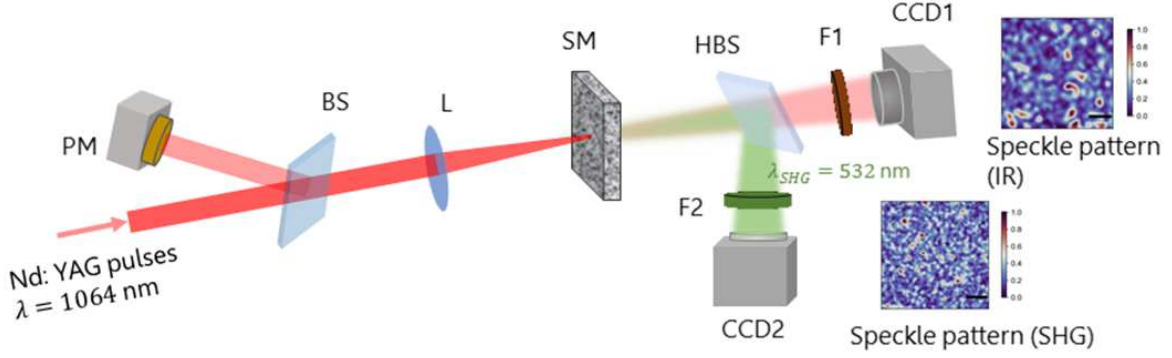


FIG. 1. Schematic setup of the experiment. Notations, BS: Beam Splitter, PM: Power Meter, L: Lens, SM: Scattering Medium, HBS: Harmonic Beam Splitter, F1: Laser line filter at $\lambda = 1064$ nm, F2: Laser line filter at $\lambda = 532$ nm, CCD1: Charged Coupled Device with InGaAs detector, CCD2: Charged Coupled Device with Silicon detector. Two experimental speckle patterns for fundamental (hereafter referred to as IR, $\lambda = 1064$ nm) and second harmonic generated (hereafter referred to as SHG, $\lambda = 532$ nm) light are shown here while the adjacent color bars indicate the normalized intensity scale.

free path for fundamental light [32]. In another study [33], angular correlations in second-harmonic speckle under dual-beam excitation were presented in a medium of LiNbO₃ microcrystals.

In this article, we report our experimental and theoretical studies on intensity-dependent decorrelation in speckle patterns produced by a second-order nonlinear disordered medium. Specifically, we show that the fundamental and second harmonic speckle patterns produced by successive incident pulses exhibit strong correlations at low input power which drop at higher power. The correlation between fundamental speckle patterns remains high compared to the second harmonic. The decay rate of the average correlation with increasing power is larger in the second harmonic speckles than in the fundamental speckles. To understand the decorrelation process, we build a theoretical model that traces the propagation of the linear field, followed by the conversion to second harmonic, finally followed by the propagation of the second harmonic. The model is in excellent qualitative agreement with the experimental results. The theoretical model is also backed up with a Monte Carlo computation, which sheds light on two contributions to the decorrelation process, namely, the decorrelation during the generation of the second-harmonic, and that due to the propagation thereof.

I. EXPERIMENTS

A. Experimental Setup

Towards the experiment, commercially available KDP (Potassium Dihydrogen Phosphate, @ EMSURE ACS) crystal grains were adopted as our nonlinear material. Initially, the grain sizes ranged from ~ 2 mm to 3 mm and were uneven in shape. The grains were subjected to

a ball milling process creating a fine powder of KDP, with particle sizes ranging from 2 to 8 μ m. The distribution of grain sizes approximately followed a log-normal distribution with a peak at 3.11 μ m and variance of 1.25 μ m. For the speckle measurement, we prepared two opaque slabs (thickness $\sim 510 \pm 15$ μ m and $\sim 680 \pm 20$ μ m) of KDP micro-crystals, and the slabs were sandwiched between two microscopic slides of thickness $\sim 170 \pm 5$ μ m. A coherent backscattering (CBS) [34, 35] experiment estimated the transport mean free path (ℓ_t) of the slabs, and the estimated values were approximately 352 μ m and 169 μ m at $\lambda = 1064$ nm and $\lambda = 532$ nm respectively. Fig. 1 illustrates the schematic of the experimental setup for the speckle correlations measurements.

Nd:YAG laser pulses (EKSPLA, PL2143B, pulse width ~ 30 ps) with the fundamental wavelength of $\lambda = 1064$ nm (hereafter referred to as IR), were chosen as our input beam. A glass wedge was introduced in the incident path to direct a small fraction ($\sim 4\%$) of the beam to a power meter (PM, Ophir Optonics, resolution: 10 μ W) for the input power measurement. The residual beam was then focused onto the scattering medium (SM) through a lens (L) of focal length 10 cm. To avoid damage to the sample, it was placed slightly away from the focus. The transmitted light consisted of both the fundamental and second harmonic light (here referred to as SHG, $\lambda = 532$ nm). A harmonic beam splitter (HBS) was employed to separate out the two components. The transmitted (IR) and reflected (SHG) lights from the HBS were then directed to the CCD1 and CCD2 respectively. The CCD1 was an InGaAs detector (SWIR camera, Photonic Science, UK) with pixel dimension 30 μ m \times 30 μ m while the CCD2 was a silicon detector (iXon Ultra 897, Andor technology) with pixel dimension 16 μ m \times 16 μ m. A laser line filter (F1) at $\lambda = 1064$ nm was added in front of the CCD1 to block any unwanted SHG photon. Similarly, a laser line filter (F2) at $\lambda = 532$ nm was placed in

front of the CCD2. The laser fired at a repetition rate of 1 Hz, and simultaneous measurements of the pulse power and the corresponding IR and SHG speckle patterns were made.

B. Results

An intense pulse of laser light impacts the disordered sample and imparts certain radiation pressure, which causes the particles to be displaced from their original position. Overall, the disorder configuration at the input face is modified, in proportion to the pump power. See Supplemental Document, Sec. I for details. Since the disorder configuration changes with every impacting optical pulse, it is imperative to avoid cumulative reconfigurations happening through multiple pump pulses. Therefore, we only grab two successive speckle patterns in two consecutive pump pulses, and then translate the sample so as to illuminate a different location on the sample. The homogeneity of disorder strength was constant across the total area, as also certified by the systematic variation in the results. The correlation coefficient between two speckle patterns A and B (both $m \times n$ matrices) was calculated as

$$C_{\text{expe}} = \frac{\sum_{i=1}^m \sum_{j=1}^n (A_{ij} - \bar{A})(B_{ij} - \bar{B})}{\sqrt{(\sum_{i=1}^m \sum_{j=1}^n (A_{ij} - \bar{A})^2)(\sum_{i=1}^m \sum_{j=1}^n (B_{ij} - \bar{B})^2)}} \quad (1)$$

where the over-bar represents the mean of the matrix.

Initial two consecutive speckle patterns of IR and SHG at an input power of 10.5 mW are presented in Fig. 2 (a,b) and (c,d) respectively. Obvious agreement between (a) and (b) is seen, with the yellow circles emphasizing the regions of clear similarity. For the SHG wavelength, there are no similarities in the speckle patterns between two consecutive pulses, indicating strong decorrelation within two pulses. The correlation coefficient $\langle C_{\text{expe}} \rangle$ was averaged over 10 sets of speckle patterns, each grabbed at a different location on the sample at the same pump intensity.

Figure 3 reveals the variant decorrelation with pump power for the fundamental and second-harmonic light. A monotonic decrease in the correlation coefficient is observed in both samples of thicknesses $L = 510 \mu\text{m}$ and $L = 680 \mu\text{m}$. At low powers, up to about 15 mW, the correlation drops rapidly, where-after the rate reduces with further increase in power. It can be expected to asymptotically approach zero. To compare the qualitative rate of decorrelation between IR and SHG, we calculate the slopes of the two curves for each point and plot them in Fig. 3(c). For $L = 510 \mu\text{m}$ and IR light, the slope initially drops indicating a slowing down of the decorrelation with increasing power. Subsequently, it rises monotonically. For the SHG light, an initially static slope is seen to rise monotonically and then saturate at highest power. For the thicker sample, the trends are very similar. The intersection between the blue and red curves

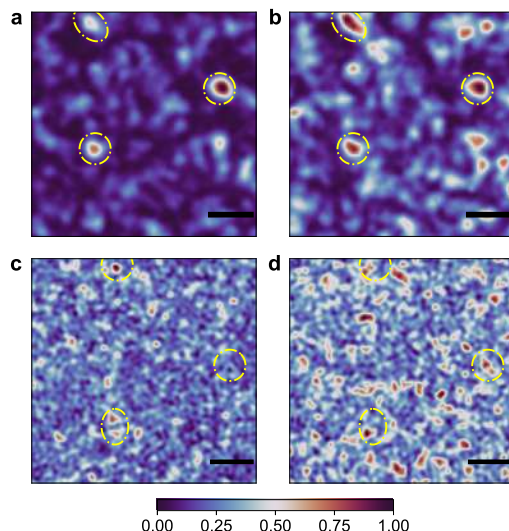


FIG. 2. Initial two consecutive speckle patterns of IR [(a) and (b)] and SHG [(c) and (d)] scattered from a $510 \mu\text{m}$ thick sample at an input power of 10.53 mW. IR speckle shows higher correlation (0.71), and the marked regions with yellow circles emphasize the agreement. On the contrary, the correlation for SHG light is observed to be low (0.23), and any regions arbitrarily chosen in the pattern (yellow circles) do not show visible agreement. Color bar indicates normalized intensity. The scale bar represents $600 \mu\text{m}$.

indicates the pump power where the decorrelation rates are same. Evidently, the two curves intersect at a lower pump power for the thicker sample. The slopes of the two curves represent the valuable diagnostic for comparing with the theoretical model, which is discussed later.

The source of the fluctuating speckle pattern can be traced to the radiation pressure of the incident pulses, which induces displacements in the scatterers in random directions. This was experimentally verified in our earlier study wherein we showed the decrease in speckle contrast with pump power [36]. A given absolute displacement of the scatterers amounts to a smaller relative displacement with respect to the wavelength for the IR light, as compared to the SHG light. However, the origin of the behavior of decorrelation seen in Figure 3 is not obvious, and needs to be rigorously evaluated. This is carried out in the next section.

II. THEORETICAL MODEL

In parallel to the experiment, we have developed a theoretical model based on coupled transport equations for the linear ($\lambda = 1064 \text{ nm}$) and second harmonic ($\lambda = 532 \text{ nm}$) lights. This model provides physical insights on the origin of the faster decorrelation for the second harmonic speckle compared to the decorrelation of the linear speckle. Before deriving the model, we first focus on the correlation function defined in Eq. (1). It can also be

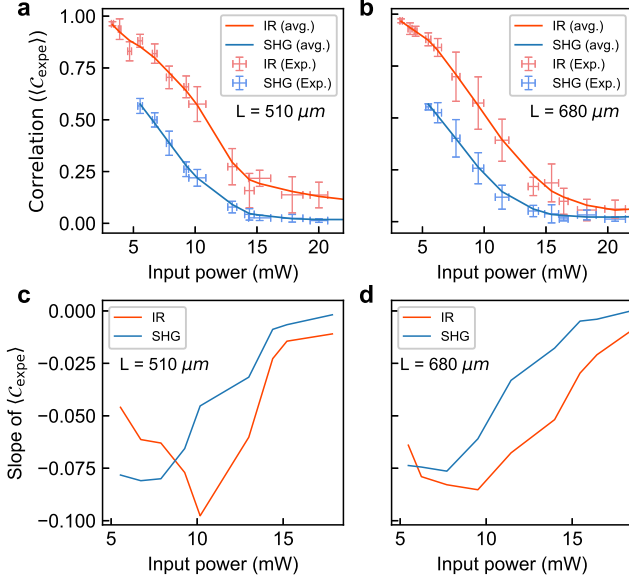


FIG. 3. Correlation coefficient between first two consecutive speckle patterns of IR (red markers) and SHG (blue markers) light as a function of input power of the fundamental light, calculated from measured speckle patterns. The solid lines are obtained after smoothing the experimental data. The data are measured on two different samples with thickness $L = 510 \mu\text{m}$ (a) and $L = 680 \mu\text{m}$ (b). Slopes of $\langle C_{\text{expe}} \rangle_{\text{IR}}$ and $\langle C_{\text{expe}} \rangle_{\text{SHG}}$ calculated on each power value for the two samples are shown in (c) for $L = 510 \mu\text{m}$ and (d) for $L = 680 \mu\text{m}$.

written as

$$C_{\text{expe}} = \frac{\int_{\text{CCD}} \delta I(\mathbf{r}) \delta \tilde{I}(\mathbf{r}) d\mathbf{r}}{\left[\int_{\text{CCD}} \delta I^2(\mathbf{r}) d\mathbf{r} \int_{\text{CCD}} \delta \tilde{I}^2(\mathbf{r}) d\mathbf{r} \right]^{1/2}} \quad (2)$$

where $\delta I = I - \bar{I}$, I being the intensity and $\bar{I} = \int_{\text{CCD}} I(\mathbf{r}) d\mathbf{r}$. \tilde{I} denotes the intensity once the scatterers have moved due to radiation pressure. It is important to note that this correlation function does not correspond to the correlation of speckle patterns at different times but measures the correlation between the speckles produced by two slightly different disorder configurations, the scatterer displacements being induced by the radiation pressure effect. Assuming ergodicity, we can replace the integration over the pixels of the CCD camera by a statistical average over all possible disorder configurations which is denoted by $\langle \cdot \rangle$. Moreover, we consider that the statistical properties of the medium are the same after the displacements of the scatterers, i.e. $\langle I \rangle = \langle \tilde{I} \rangle$. Next, we assume that the field has Gaussian statistics (or equivalently that the speckles are fully developed), which is valid in the regime $k_0 \ell_s \gg 1$, $k_0 = \omega/c = 2\pi/\lambda$ being the wave number and ℓ_s the scattering mean-free path. This implies that $\langle \delta I^2 \rangle = \langle I \rangle^2$. The correlation

function in Eq. (2) becomes $C_{\text{expe}} \sim C_I - 1$ where

$$C_I(\mathbf{r}) = \frac{\langle I(\mathbf{r}) \tilde{I}(\mathbf{r}) \rangle}{\langle I(\mathbf{r}) \rangle^2}. \quad (3)$$

Finally, we also have $C_I = 1 + |C|^2$ where C is the field-field correlation function given by

$$C(\mathbf{r}) = \frac{\langle E(\mathbf{r}) \tilde{E}^*(\mathbf{r}) \rangle}{\langle E(\mathbf{r}) E^*(\mathbf{r}) \rangle}, \quad (4)$$

E being the electric field and the superscript $*$ denoting the complex conjugate. It is important to note that we make the assumption of a scalar field for the sake of simplicity. This can be justified in the multiple scattering regime where the field can be considered to be fully depolarized [37]. We finally have

$$C_{\text{expe}} \sim |C|^2. \quad (5)$$

The problem of estimating theoretically C_{expe} now reduces to the computation of C for two different frequencies, i.e. ω for the linear beam and 2ω for the second harmonic one. The purpose of the next subsections is to develop a transport model for C . We present only the important steps, the full derivation from first principles being described in the Supplemental Document, Sec. II.

A. Disorder model

The real samples are composed of packed KDP crystal grains of different sizes and shapes. Thus the most relevant and simple disorder model consists in a fluctuating continuous and real (no absorption) permittivity $\epsilon(\mathbf{r})$. The disorder microstructure is then characterized by a spatial correlation function chosen to be Gaussian, in the form

$$C_\epsilon(|\mathbf{r} - \mathbf{r}'|, \omega) = \langle \delta\epsilon(\mathbf{r}, \omega) \delta\epsilon(\mathbf{r}', \omega) \rangle = |\Delta\epsilon(\omega)|^2 \exp \left[-\frac{|\mathbf{r} - \mathbf{r}'|^2}{2\ell^2} \right]. \quad (6)$$

In this equation, $\delta\epsilon(\mathbf{r}, \omega) = \epsilon(\mathbf{r}, \omega) - \langle \epsilon(\mathbf{r}, \omega) \rangle$ is the fluctuating part of the permittivity, $|\Delta\epsilon(\omega)|^2$ is the amplitude of the correlation and ℓ is the correlation length. $|\Delta\epsilon(\omega)|^2$ depends on frequency since the permittivity ϵ is dispersive. However, ℓ involves only the geometrical structure of the disorder and thus does not depend on frequency. The $\chi^{(2)}$ nonlinearity is supposed to be correlated in a similar way.

B. Linear regime

We first consider the linear regime ($\lambda = 1064 \text{ nm}$) corresponding to propagation at the fundamental frequency

ω . We use an approach similar to that in Ref. [38] developed in the context of the Diffusing-Wave Spectroscopy (DWS). The most important point concerns the selections of the scattering paths followed by the field E and its complex conjugate E^* that dominate in the expression of the correlation function C . In a dilute medium such that $k_0 \ell_s \gg 1$, the leading contribution corresponds to E and E^* following the same scattering sequences. These sequences can be represented by the diagram

$$\begin{array}{c} E(\mathbf{r}, \omega) \text{---} \bigcirc \text{---} \bigcirc \text{---} \bigcirc \text{---} E_0 \\ | \quad | \quad | \\ \tilde{E}^*(\mathbf{r}, \omega) \text{---} \bigcirc \text{---} \bigcirc \text{---} \bigcirc \text{---} E_0^* \end{array} \quad (7)$$

with an arbitrary number of scattering events [39]. In these so-called ladder diagrams, the circles represent the scattering events, the thick solid lines correspond to the Green functions modelling the field propagation between scattering events and the thick dashed lines denote the incident field. The upper (bottom) line describes the propagation of E (\tilde{E}^*) respectively and the thin dashed vertical lines represent the disorder correlation C . It is important to note that in the model of continuous disorder, the circles do not represent real scatterers (grains) but scattering events connected by the correlation function C . The width ℓ of the correlation function C is however on the order of the grain size. The ladder shape of this dominant diagram implies that there is always constructive interference between the field E and its complex conjugate \tilde{E}^* . Thus the problem of computation of C reduces to the problem of solving a radiative transport equation [40]

$$\begin{aligned} & \left[\mathbf{u} \cdot \nabla_{\mathbf{r}} + \frac{1}{\ell_s(\omega)} \right] \tilde{I}(\mathbf{r}, \mathbf{u}, \omega) \\ &= \frac{1}{\ell_s(\omega)} \int p(\mathbf{u}, \mathbf{u}', \omega) g(\mathbf{r}, \mathbf{u}, \mathbf{u}', \omega) \tilde{I}(\mathbf{r}, \mathbf{u}', \omega) d\mathbf{u}'. \end{aligned} \quad (8)$$

where $\tilde{I}(\mathbf{r}, \mathbf{u}, \omega)$ is the specific intensity, that can be seen as the radiative flux at position \mathbf{r} , in direction \mathbf{u} and at frequency ω . More precisely, it can be shown from first principles that it is given by the Wigner transform of the field. In our context (scatterer displacements), it reads

$$\delta(k - k_0) \tilde{I}(\mathbf{r}, \mathbf{u}, \omega) = \int \left\langle E\left(\mathbf{r} + \frac{\mathbf{s}}{2}, \omega\right) \tilde{E}^*\left(\mathbf{r} - \frac{\mathbf{s}}{2}, \omega\right) \right\rangle \times e^{-ik\mathbf{u} \cdot \mathbf{s}} d\mathbf{s}. \quad (9)$$

Thus, solving for \tilde{I} gives a direct access to the field-field correlation function C . Equation (8) is very similar to the standard Radiative Transfer Equation (RTE) [41] except that it includes an additional function $g(\mathbf{r}, \mathbf{u}, \mathbf{u}', \omega)$ that represents the decorrelation of the field at each scattering event due to the motion of scatterers. It is given by

$$g(\mathbf{r}, \mathbf{u}, \mathbf{u}', \omega) = \int e^{-ik_0(\mathbf{u} - \mathbf{u}') \cdot \Delta} f(\mathbf{r}, \Delta) d\Delta \quad (10)$$

where \mathbf{u} and \mathbf{u}' are unit vectors representing the scattered and incoming directions for a given scattering process. $f(\mathbf{r}, \Delta)$ is the probability density to have a displacement Δ of a scatterer at the position \mathbf{r} . The position dependence is required since this displacement is induced by the radiation pressure that can be heterogeneous inside the medium (in particular at small depths). Eq. (10) can be interpreted as follows: the decorrelation is due to the phase shift (Doppler shift) averaged over all accessible displacements for a scatterer. As a simple model, we consider that the amplitude of the displacement is proportional to the specific intensity which leads to

$$\begin{aligned} f(\mathbf{r}, \Delta) &= \delta \left[\Delta - \beta I \left(\mathbf{r}, \frac{\Delta}{\Delta}, \omega \right) \right] \\ &\times \left[\beta^2 \int I(\mathbf{r}, \mathbf{u}, \omega)^2 d\mathbf{u} \right]^{-1} \end{aligned} \quad (11)$$

where β is factor taking into account the link between the displacement and the value of the specific intensity. In the following β will be considered as a scaling parameter. In Eq. (11), $I(\mathbf{r}, \mathbf{u}, \omega)$ is the specific intensity without any displacements. Finally $p(\mathbf{u}, \mathbf{u}', \omega)$ is the phase function representing the part of energy incident from direction \mathbf{u}' and scattered into direction \mathbf{u} . For the Gaussian disorder considered here, it is given by

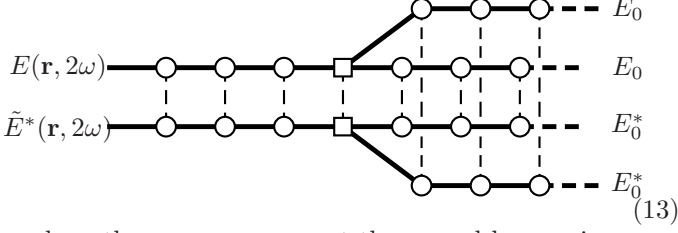
$$p(\mathbf{u}, \mathbf{u}', \omega) \propto p(k_0 |\mathbf{u} - \mathbf{u}'|) \quad \text{where} \quad p(q) = \exp \left[-\frac{q^2 \ell^2}{2} \right] \quad (12)$$

and normalized such that $\int p(\mathbf{u}, \mathbf{u}', \omega) d\mathbf{u}' = 1$. Equation (8) can easily be interpreted using a random walk approach. Indeed, light undergoes a random walk whose average step is given by the scattering mean-free path $\ell_s(\omega)$ and whose angular distribution at each scattering event is given by the phase function $p(\mathbf{u}, \mathbf{u}', \omega)$. A phase shift is introduced between the fields at each scattering event due to the displacement of the scatterers as described by the function $g(\mathbf{r}, \mathbf{u}, \mathbf{u}', \omega)$.

C. Second harmonic regime

We now address the question of the generation and propagation of the second harmonic light. As it is usually done in homogeneous materials, we use a perturbative approach in order to compute the field at 2ω from the field at ω . The full process can be broken down into three steps. First the linear field at ω propagates inside the material. Second, it is converted to second harmonic on an arbitrary scatterer. And finally, this process is followed by the propagation of the second harmonic field. The same sequence of processes also applies to the complex conjugate of the field. From this sequence, the most important point is still here the identification of the leading diagram taking into account the non-linearity. It is

given by



where the squares represent the second harmonic generation process. We could assume the non-linear processes for E and \tilde{E}^* to occur at two positions with an arbitrary distance between them. However, this would lead to the propagation of the correlations $\langle E(\mathbf{r}, \omega) \tilde{E}^*(\mathbf{r}, 2\omega) \rangle$ or $\langle E(\mathbf{r}, 2\omega) \tilde{E}^*(\mathbf{r}, \omega) \rangle$ which are supposed to vanish since they involve fields at two different frequencies. The generations of the second harmonic sources for E and \tilde{E}^* are then confined in a small volume with typical size ℓ . The relevance of the dominant diagram responsible for the second harmonic correlation has to be carefully checked. For that purpose, we have performed ab initio numerical simulations that are presented in the Supplemental Document, Sec. III. Finally, the diagram of Eq. (13) can be interpreted the following way: the right part represents the propagation of two specific intensities at frequency ω obeying Eq. (8) and the left part represents the propagation of the specific intensity at frequency 2ω . It is given by the following non-linear RTE

$$\begin{aligned} & \left[\mathbf{u} \cdot \nabla_{\mathbf{r}} + \frac{1}{\ell_s(2\omega)} \right] \tilde{I}(\mathbf{r}, \mathbf{u}, 2\omega) \\ &= \frac{1}{\ell_s(2\omega)} \int p(\mathbf{u}, \mathbf{u}', 2\omega) g(\mathbf{r}, \mathbf{u}, \mathbf{u}', 2\omega) \tilde{I}(\mathbf{r}, \mathbf{u}', 2\omega) d\mathbf{u}' \\ &+ \alpha \iint p_{\text{SHG}}(\mathbf{u}, \mathbf{u}', \mathbf{u}'', \omega) g_{\text{SHG}}(\mathbf{r}, \mathbf{u}, \mathbf{u}', \mathbf{u}'', \omega) \\ &\quad \times \tilde{I}(\mathbf{r}, \mathbf{u}', \omega) \tilde{I}(\mathbf{r}, \mathbf{u}'', \omega) d\mathbf{u}' d\mathbf{u}''. \quad (14) \end{aligned}$$

This equation is the main theoretical result of this work. It shows that the second harmonic specific intensity follows a similar transport equation as the fundamental intensity [Eq. (8)], but with a source term describing the non-linear conversion process. Its physical interpretation is very simple: Light propagates first at frequency ω which is described by the specific intensity $\tilde{I}(\mathbf{r}, \mathbf{u}'', \omega)$ solution to Eq. (8). Then a SHG process occurs which creates a source at frequency 2ω , the amplitude of which is given by the product of two specific intensities at ω . Finally, propagation at 2ω is described by the specific intensity $\tilde{I}(\mathbf{r}, \mathbf{u}', 2\omega)$ that follows Eq. (14). In this expression, α is a factor that takes into account all constants involved in the SHG process such as $\chi^{(2)}$. $p_{\text{SHG}}(\mathbf{u}, \mathbf{u}', \mathbf{u}'', \omega)$ is the SHG phase function. It involves three unit vectors. \mathbf{u}' and \mathbf{u}'' corresponds to the incoming directions of the two specific intensities at ω and \mathbf{u} is the outgoing direction of the specific intensity at 2ω . In the case of the correlated

disorder we consider here, we have

$$p_{\text{SHG}}(\mathbf{u}, \mathbf{u}', \mathbf{u}'', \omega) \propto p(k_0 | 2\mathbf{u} - \mathbf{u}' - \mathbf{u}'' |) \quad (15)$$

with $\int p_{\text{SHG}}(\mathbf{u}, \mathbf{u}', \mathbf{u}'', \omega) d\mathbf{u}' d\mathbf{u}'' = 1$. \mathbf{u} appears with a factor two since it corresponds to the non-linear specific intensity direction. $g_{\text{SHG}}(\mathbf{u}, \mathbf{u}', \mathbf{u}'', \omega)$ is the decorrelation function given by

$$g_{\text{SHG}}(\mathbf{r}, \mathbf{u}, \mathbf{u}', \mathbf{u}'', \omega) = \int e^{-ik_0(2\mathbf{u} - \mathbf{u}' - \mathbf{u}'') \cdot \Delta} f(\mathbf{r}, \Delta) d\Delta. \quad (16)$$

It still corresponds to the decorrelation induced by a Doppler shift involving three beams, i.e. two incoming beams at frequency ω in directions \mathbf{u}' and \mathbf{u}'' and one outgoing beam at frequency 2ω in direction \mathbf{u} .

D. Numerical simulations

In order, to solve the system of Eqs. (8) and (14), we have developed a Monte Carlo scheme which can be seen as a random walk process inside the material [42]. Three Monte Carlo simulations are performed in a slab geometry of thickness L under plane-wave illumination at normal incidence. The first is used to compute $I(\mathbf{r}, \mathbf{u}, \omega)$, the specific intensity in the absence of displacement of the scatterers. This is required in order to compute the probability density $f(\mathbf{r}, \Delta)$ to have a displacement Δ at position \mathbf{r} . The second Monte Carlo simulation is used to compute $\tilde{I}(\mathbf{r}, \mathbf{u}, \omega)$, the specific intensity associated with the correlation function at ω . Finally, a last simulation is performed in order to compute $\tilde{I}(\mathbf{r}, \mathbf{u}, 2\omega)$, the specific intensity associated with the correlation function at 2ω . More precisely, the correlation functions are computed from the energy density at the output interface in transmission, i.e.

$$C(\omega) = \frac{\int \tilde{I}(z = L, \mathbf{u}, \omega) d\mathbf{u}}{\int I(z = L, \mathbf{u}, \omega) d\mathbf{u}}, \quad (17)$$

$$C(2\omega) = \frac{\int \tilde{I}(z = L, \mathbf{u}, 2\omega) d\mathbf{u}}{\int I(z = L, \mathbf{u}, 2\omega) d\mathbf{u}}. \quad (18)$$

This computations are performed for different incident intensities I_0 (or different incident powers $\langle P \rangle$) meaning different probability density $f(\mathbf{r}, \Delta)$ which correspond to different radiation pressures. Regarding the numerical parameters, it is important to keep in mind that the KDP powder used in the experiment has crystal grains of different sizes ranging from $2\mu\text{m}$ to $8\mu\text{m}$. This makes difficult the choice of the correlation length ℓ . However we have tested several values showing that this is not a crucial parameter. Since the particles are large compared to the wavelength, we have chosen $k_0\ell = 3$ for the results presented in Fig. 4. This gives the anisotropy factors $g(\omega) = 0.89$ and $g(2\omega) = 0.97$. The thickness of the medium L as well as the transport mean-free paths $\ell_t = \ell_s/(1 - g)$ take the values measured experimentally, which gives $k_0L = 4016$, $k_0\ell_t(\omega) = 2079$ and

$k_0 \ell_t(2\omega) = 998$. This finally leads to the normalized scattering mean-free paths $k_0 \ell_s(\omega) = 229$ and $k_0 \ell_s(2\omega) = 30$.

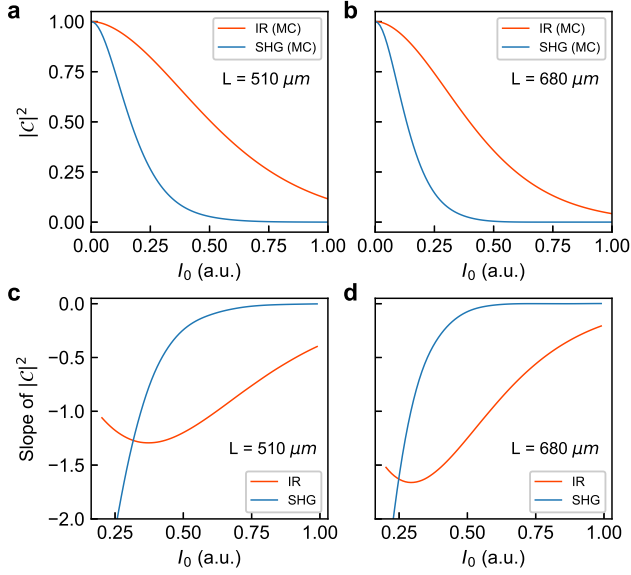


FIG. 4. Monte Carlo (MC) simulated correlation functions $|C|^2$ for the linear (red solid line) and second harmonic (blue solid line) beams as a function of the incident intensity I_0 in arbitrary units. (a) $L = 510 \mu\text{m}$, (b) $L = 680 \mu\text{m}$. The range of I_0 is chosen such that the extreme values of the linear correlation $|C(\omega)|^2$ are in agreement with the experimental values $C_{\text{expe}}(\omega)$ presented. Slopes of $|C(\omega)|^2$ and $|C(2\omega)|^2$ calculated on each power value for the two samples are shown in (c) $L = 510 \mu\text{m}$ and (d) $L = 680 \mu\text{m}$. A qualitative agreement is immediately seen with the experimental behavior in Fig. 3

We can observe that the results shown in Fig. 3 are reproduced qualitatively. The second-harmonic beam decorrelates faster than that of the fundamental frequency. The slopes of the decorrelation curves also reproduce the same trends seen in experiments, for most part of the input power range. The IR light shows a reducing slope followed by a rise at a certain pump power, while the frequency-doubled light shows a steady rise followed by a saturation region. Barring a minor difference at low powers, the experimental data exhibit the same behavior. The crossing of the two slope curves also happens at a lower pump power in the thicker sample, as seen in the experiments. The agreement with the experiments is very clear qualitatively, but is not quantitative. The main reason should probably be investigated in the dependence of the probability density f on the specific intensity I . Building this relationship is not a trivial task and is out of the scope of the present work. A second potential effect that has been neglected so far, is the role of the refractive index mismatch at the interfaces of the slab. In the Monte Carlo simulation we have verified that this does not change substantially the results up to a refractive index $n = 2$.

The faster decorrelation of the second harmonic

speckle can be explained through two different mechanisms: The first one corresponds to the decorrelation when the second harmonic light is generated which is represented by $g_{\text{SHG}}(\mathbf{r}, \mathbf{u}, \mathbf{u}', \omega)$. Its dependence on the three different directions through the relation $2\mathbf{u} - \mathbf{u}' - \mathbf{u}''$ favors a faster decorrelation. The second mechanism is due to the propagation of the second harmonic field. The factor of two in $g(\mathbf{r}, \mathbf{u}, \mathbf{u}', 2\omega)$ also makes the correlation vanish faster than for the linear beam. For a small optical thickness, both effects play a role and have to be taken into account properly. This comes from the fact that photons experience few scattering events before escaping the medium and thus the decorrelations due to g_{SHG} and to g are of the same order of magnitude. On the other hand, for large optical thicknesses, many scattering events are involved and the contribution of g_{SHG} is negligible compared to that of g . Figure 5 illustrate this statement using the Monte Carlo simulations. This simple conclusion will also be easily observed in the more simple case of statistically homogeneous and isotropic displacements discussed in the next section.

E. Statistically homogeneous and isotropic displacements

Beyond the effect of radiation pressure that has been examined in this study, it is also interesting to consider a displacement probability for the scatterers that is homogeneous and isotropic, i.e. $f(\mathbf{r}, \Delta) = f(\Delta)/(4\pi\Delta^2)$. Indeed, considering large medium thicknesses compared to the transport mean-free paths, i.e. $L \gg \{\ell_t(\omega), \ell_t(2\omega)\}$, we can derive diffusion equations for the linear and second harmonic correlation functions. The derivation is detailed in the Supplemental Document, Sec. IV and leads to analytical expressions given by

$$C(\omega) = \frac{\kappa(\omega)L}{\sinh[\kappa(\omega)L]}, \quad (19)$$

$$C(2\omega) = \frac{6\mathcal{D}(\omega)}{\kappa(2\omega)L \sinh[\kappa(\omega)L]^2 \sinh[\kappa(2\omega)L]} \times \frac{\kappa(2\omega)^2 \{1 - \cosh[2\kappa(\omega)L]\} - 4\kappa(\omega)^2 \{1 - \cosh[\kappa(2\omega)L]\}}{\kappa(2\omega)^2 - 4\kappa(\omega)^2} \quad (20)$$

where

$$\kappa = \sqrt{\frac{3}{\tilde{\ell}_t \tilde{\ell}_a}}, \quad \tilde{\ell}_t = \frac{\ell_s}{1 - \tilde{g}}, \quad (21)$$

$$\frac{1}{\tilde{\ell}_a} = \frac{1}{\ell_s} \left[1 - \int p(\mathbf{u}, \mathbf{u}') g(\mathbf{u}, \mathbf{u}') d\mathbf{u}' \right], \quad (22)$$

$$\text{and } \tilde{g} = \frac{\int p(\mathbf{u}, \mathbf{u}') g(\mathbf{u}, \mathbf{u}') \mathbf{u} \cdot \mathbf{u}' d\mathbf{u}'}{\int p(\mathbf{u}, \mathbf{u}') g(\mathbf{u}, \mathbf{u}') d\mathbf{u}'}, \quad (23)$$

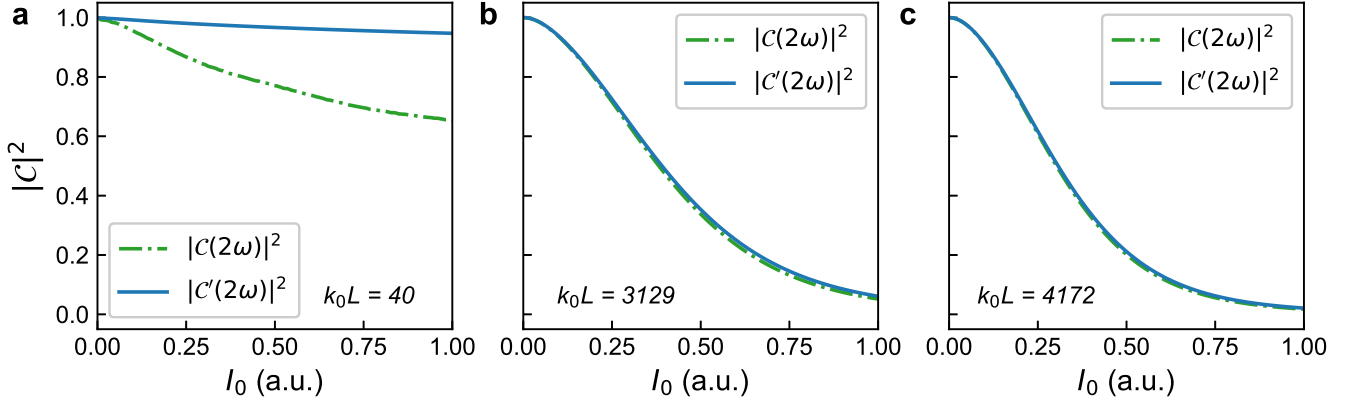


FIG. 5. Monte Carlo (MC) simulated correlation functions $|C|^2$ for the second harmonic speckles taking into account all decorrelation effects (i.e. effect of g and g_{SHG} , green dashed line) and only the decorrelation occurring during beam propagation (i.e. effect of g , blue solid line). The computations are performed for (a) $k_0 L = 40$, (b) $k_0 L = 3129$ and (c) $k_0 L = 4172$. The other parameters are the same as in Fig. 4.

all these four quantities being defined at ω and 2ω . We also have

$$\mathcal{D}(\omega) = \frac{\int p_{\text{SHG}}(\mathbf{u}, \mathbf{u}', \mathbf{u}'', \omega) g_{\text{SHG}}(\mathbf{u}, \mathbf{u}', \mathbf{u}'', \omega) d\mathbf{u} d\mathbf{u}' d\mathbf{u}''}{\int p_{\text{SHG}}(\mathbf{u}, \mathbf{u}', \mathbf{u}'', \omega) d\mathbf{u} d\mathbf{u}' d\mathbf{u}''}. \quad (24)$$

We clearly see from these expressions that the effect of the decorrelation during the propagation of the waves at ω or at 2ω can be seen as an absorption effect and are encoded in the κ functions. The decorrelation process taking place during the generation of the second harmonic light is encoded in the \mathcal{D} function. Finally these analytical expressions can be simplified in the even more particular case of isotropic scattering such that $p(\mathbf{u}, \mathbf{u}') = 1/(4\pi)$ and $p_{\text{SHG}}(\mathbf{u}, \mathbf{u}', \mathbf{u}'', \omega) = 1/(16\pi^2)$ and of a constant displacement amplitude d such that $k_0 d \ll 1$ and $f(\Delta) = \delta(\Delta - d)$. This gives

$$\kappa(\omega)L = b(\omega)k_0 d, \quad \kappa(2\omega)L = 2b(2\omega)k_0 d \quad (25)$$

$$\text{and } \mathcal{D}(\omega) = \frac{1}{8\pi} \int_{\phi=0}^{2\pi} \int_{\mu=-1}^1 \int_{\mu'=-1}^1 \text{sinc} \left[k_0 d \sqrt{6 - 4\mu - 4\mu' + 2\mu\mu' + 2\sqrt{1-\mu^2}\sqrt{1-\mu'^2} \cos \phi} \right] \times d\mu d\mu' d\phi \quad (26)$$

where $b = L/\ell_s$ is the optical thickness. These last expressions are very useful to get more insights on the decorrelation effects encoded in functions $\kappa(\omega)$, $\kappa(2\omega)$ and $\mathcal{D}(\omega)$. In particular, as already noticed in the numerical simulations, we clearly see that the decorrelation during propagation is stronger when the optical thicknesses $b(\omega)$ and $b(2\omega)$ increase which reduces the effect of $\mathcal{D}(\omega)$. In the diffusive regime considered here, $\mathcal{D}(\omega)$ can thus be replaced by its limit when $k_0 d \rightarrow 0$, i.e. $\mathcal{D}(\omega) \sim 1$.

III. DISCUSSION AND CONCLUSION

In summary, we have experimentally investigated the decorrelation of speckle patterns with increasing pump power in a second-order nonlinear disordered medium. Simultaneous speckle measurements at the fundamental and second harmonic wavelengths reveal a varying rate of decorrelation under the same incident power. The decorrelation arises from the microscopic displacements in the disorder configuration induced by the radiation pressure produced by the pump beam. In addition, the second harmonic correlation decreases faster than the fundamental. We laid the foundations of a theoretical model that accurately describes the synergy of second-order nonlinearity and light diffusion. The model demarcates the contribution of two components in the decorrelation, namely, one arising from the generation of second-harmonic light, and the other arising from the propagation thereof. For the samples and input powers employed in our experiments, the former seems to be the stronger contributor. Wider investigations of the model show that the relative strengths of the two components depend upon the degree of disorder. Towards the differences in the experimental and computed results, we have discussed qualitatively the origins as follows. The actual displacement at a location \mathbf{r} is dependent on the specific intensity at that location, and the size and shape of the particle at that location. This is too intricate a parameter to calculate, and we did not venture into it. In the theory, the sample is homogeneously disordered, and particle size is not a parameter in computing the displacement under radiation pressure. At a future stage, a distribution in the displacements may be invoked in the theory. We believe these unavoidable differences in the experimental samples and theoretical assumptions limit the agreement in the respective results. This study shades light on the subtle mechanism of non-linear conversion in disordered

media, with expected outcomes in fundamental studies in mesoscopic wave transport, as well as the design of efficient materials for non-linear generation of light.

FUNDING INFORMATION

Department of Atomic Energy, Government of India for funding for the project identification No. RTI4002 under the DAE OM No 1303/1/2020/R&D-II/DAE/5567 dated 20.8.2020; Swarnajayanti Fellowship, Department of Science and Technology, Ministry of Science and Technology, India.

This work has received support under the program “Investissements d’Avenir” launched by the French Government.

ACKNOWLEDGMENT

R.S. and S.M. acknowledge the support from Sandip Mondal and N. Sreeman Kumar during the experiment.

DISCLOSURES

The authors declare no conflicts of interest.

-
- [1] A. Ishimaru, *Wave Propagation and Scattering in Random Media* (Academic, 1978).
 - [2] D. S. Wiersma, Disordered photonics, *Nature Photonics* **7**, 188–196 (2013).
 - [3] C. Conti, L. Angelani, and G. Ruocco, Light diffusion and localization in three-dimensional nonlinear disordered media, *Phys. Rev. A* **75**, 033812 (2007).
 - [4] I. V. Shadrivov, K. Y. Bliokh, Y. P. Bliokh, V. Freilikher, and Y. S. Kivshar, Bistability of anderson localized states in nonlinear random media, *Phys. Rev. Lett.* **104**, 123902 (2010).
 - [5] A. Mafi, A brief overview of the interplay between nonlinearity and transverse anderson localization, *arXiv:1703.04011* (2017).
 - [6] Y. Sharabi, H. H. Sheinfux, Y. Sagi, G. Eisenstein, and M. Segev, Self-induced diffusion in disordered nonlinear photonic media, *Phys. Rev. Lett.* **121**, 233901 (2018).
 - [7] V. M. Agranovich and V. E. Kravtsov, Effects of weak localization of photons in nonlinear optics: Second harmonic generation, *Physics Letters A* **131**, 378 (1988).
 - [8] K. M. Yoo, S. Lee, Y. Takiguchi, and R. R. Alfano, Search for the effect of weak photon localization in second-harmonic waves generated in a disordered anisotropic nonlinear medium, *Optics Letters* **14**, 800 (1989).
 - [9] S. Faez, P. M. Johnson, D. A. Mazurenko, and A. Lagendijk, Experimental observation of second-harmonic generation and diffusion inside random media, *Journal of the Optical Society of America B* **26**, 235 (2009).
 - [10] C. I. Valencia and E. R. Méndez, Weak localization effects in the second-harmonic light scattered by random systems of particles, *Optics Communications* **282**, 1706 (2009).
 - [11] R. Savo, A. Morandi, J. S. Müller, F. Kaufmann, F. Timpu, M. R. Escalé, M. Zanini, L. Isa, and R. Grange, Broadband mie driven random quasi-phase-matching, *Nature Photonics* **14**, 740–747 (2020).
 - [12] J. S. Müller, A. Morandi, R. Grange, and R. Savo, Modeling of random quasi-phase-matching in birefringent disordered media, *Physical Review Applied* **15**, 064070 (2021).
 - [13] A. Morandi, R. Savo, J. S. Müller, S. Reichen, and R. Grange, Multiple scattering and random quasi-phase-matching in disordered assemblies of LiNbO₃ nanocubes, *ACS Photonics* **9**, 1882–1888 (2022).
 - [14] J. W. Goodman, *Speckle Phenomena in Optics: Theory and Applications* (Roberts & Company, 2007).
 - [15] S. Feng, C. Kane, P. A. Lee, and A. D. Stone, Correlations and fluctuations of coherent wave transmission through disordered media, *Physical Review Letters* **61**, 834 (1988).
 - [16] I. Freund, M. Rosenbluh, and S. Feng, Memory effects in propagation of optical waves through disordered media, *Physical Review Letters* **61**, 2328 (1988).
 - [17] S. Schott, J. Bertolotti, J.-F. Léger, L. Bourdieu, and S. Gigan, Characterization of the angular memory effect of scattered light in biological tissues, *Optics Express* **23**, 13505 (2015).
 - [18] B. Judkewitz, R. Horstmeyer, I. M. Vellekoop, I. N. Papadopoulos, and C. Yang, Translation correlations in anisotropically scattering media, *Nature Physics* **11**, 684–689 (2015).
 - [19] G. Osnabrugge, R. Horstmeyer, I. N. Papadopoulos, B. Judkewitz, and I. M. Vellekoop, Generalized optical memory effect, *Optica* **4**, 886 (2017).
 - [20] H. Liu, Z. Liu, M. Chen, S. Han, and L. V. Wang, Physical picture of the optical memory effect, *Photonics Research* **7**, 1323 (2019).
 - [21] J. Bertolotti, E. G. van Putten, C. Blum, A. Lagendijk, W. L. Vos, and A. P. Mosk, Non-invasive imaging through opaque scattering layers, *Nature* **491**, 232–234 (2012).
 - [22] O. Katz, P. Heidmann, M. Fink, and S. Gigan, Non-invasive single-shot imaging through scattering layers and around corners via speckle correlations, *Nature Photonics* **8**, 784–790 (2014).
 - [23] N. Fayard, A. Cazé, R. Pierrat, and R. Carminati, Intensity correlations between reflected and transmitted speckle patterns, *Physical Review A* **92**, 033827 (2015).
 - [24] N. Fayard, A. Goetschy, R. Pierrat, and R. Carminati, Mutual information between reflected and transmitted speckle images, *Physical Review Letters* **120**, 073901 (2018).
 - [25] I. Starshynov, A. M. Paniagua-Díaz, N. Fayard, A. Goetschy, R. Pierrat, R. Carminati, and J. Bertolotti, Non-gaussian correlations between reflected and transmitted intensity patterns emerging from opaque disordered media, *Physical Review X* **8**, 021041 (2018).
 - [26] A. Fleming, C. Conti, T. Vettengburg, and A. D. Falco, Nonlinear optical memory effect,

- Optics Letters **44**, 4841 (2019).
- [27] S. E. Skipetrov and R. Maynard, Instabilities of waves in nonlinear disordered media, Phys. Rev. Lett. **85**, 736 (2000).
 - [28] S. E. Skipetrov, Instability of speckle patterns in random media with noninstantaneous kerr nonlinearity, Optics Letters **28**, 646 (2003).
 - [29] S. E. Skipetrov, Dynamic instability of speckle patterns in nonlinear random media, Journal of the Optical Society of America B **21**, 168 (2004).
 - [30] B. Grémaud and T. Wellens, Speckle instability: Coherent effects in nonlinear disordered media, Phys. Rev. Lett. **104**, 133901 (2010).
 - [31] I. I. Smolyaninov, A. Gungor, and C. C. Davis, Experimental observation of speckle instability in a two-dimensional disordered medium, Metamaterials **4**, 207 (2010).
 - [32] J. F. de Boer, A. Lagendijk, R. Sprik, and S. Feng, Transmission and reflection correlations of second harmonic waves in nonlinear random media, Physical Review Letters **71**, 3947 (1993).
 - [33] T. Ito and M. Tomita, Speckle correlation measurement in a disordered medium observed through second-harmonics generation, Phys. Rev. E **69**, 036610 (2004).
 - [34] P.-E. Wolf and G. Maret, Weak localization and coherent backscattering of photons in disordered media, Physical Review Letters **55**, 2696 (1985).
 - [35] E. Akkermans, P. E. Wolf, and R. Maynard, Coherent backscattering of light by disordered media: Analysis of the peak line shape, Physical Review Letters **56**, 1471 (1986).
 - [36] R. Samanta and S. Mujumdar, Intensity-dependent speckle contrast of second harmonic light in a nonlinear disordered medium, Applied Optics **59**, 11266 (2020).
 - [37] K. Vynck, R. Pierrat, and R. Carminati, Polarization and spatial coherence of electromagnetic waves in uncorrelated disordered media, Phys. Rev. A **89**, 013842 (2014).
 - [38] R. Pierrat, Transport equation for the time correlation function of scattered field in dynamic turbid media, J. Opt. Soc. Am. A **25**, 2840 (2008).
 - [39] D. V. Kupriyanov, I. M. Sokolov, and M. D. Havey, Mesoscopic coherence in light scattering from cold, optically dense and disordered atomic systems, Physics Reports **671**, 1 (2017).
 - [40] S. M. Rytov, Y. A. Kravtsov, and V. I. Tatarskii, *Principles of Statistical Radiophysics*, Vol. 4 (Springer-Verlag, Berlin, 1989).
 - [41] S. Chandrasekhar, *Radiative Transfer* (Dover, New York, 1950).
 - [42] R. Siegel and J. R. Howell, *Thermal radiation heat transfer*, 3rd ed. (Hemisphere, Taylor and Francis, 1992).

Speckle decorrelation in fundamental and second-harmonic light scattered from nonlinear disorder: supplemental document

Rabisankar Samanta,¹ Romain Pierrat,^{2,*} Rémi Carminati,^{2,3} and Sushil Mujumdar^{1,†}

¹*Nano-optics and Mesoscopic Optics Laboratory, Tata Institute of Fundamental Research, 1 Homi Bhabha Road, Mumbai, 400 005, India*

²*Institut Langevin, ESPCI Paris, PSL University, CNRS, 1 rue Jussieu, 75005 Paris, France*

³*Institut d'Optique Graduate School, Université Paris-Saclay, F-91127 Palaiseau, France*

(Dated: August 4, 2022)

CONTENTS

I. A different experiment to validate particle movement due to laser radiation pressure	1
II. Transport model derivation	3
A. Disorder model and scattering potential	3
B. Self-energy and intensity vertex	3
C. Linear regime	5
D. Second harmonic regime	6
III. Validity check from ab initio simulations	8
A. Coupled-dipole model	8
1. Linear regime	8
2. Non-linear regime	9
B. Monte Carlo scheme	9
C. Numerical result comparison	9
IV. Diffusion limit	10
A. Linear regime	10
B. Second harmonic regime	12
C. Comparison to Monte Carlo simulations	14
References	14

I. A DIFFERENT EXPERIMENT TO VALIDATE PARTICLE MOVEMENT DUE TO LASER RADIATION PRESSURE

We have carried out experiments to demonstrate the scatterer displacements are due to radiation pressure. Specifically, a stabilized frequency, low power CW laser (HeNe, $\lambda = 632.8\text{nm}$) was made incident onto the sample simultaneously with the pump. The phase stability of the HeNe laser was confirmed by performing a simple experiment. First, we focused the HeNe laser on a ground glass diffuser and subsequently captured the transmitted speckle pattern on a CMOS camera over 30 min at an interval of 1 min. In Fig. 1, we plot the speckle correlation calculated with respect to the initial speckle pattern. We observed that the correlation coefficient always stays close to the ideal value 1 (indicated by red dashed line) which proves our HeNe laser was to be highly stable.

It is well known that the speckle pattern produced by a scattering medium remains static if the scatterers of the medium do not move. A schematic of the experimental setup is depicted in Fig. 2. Nd:YAG laser pulses (pulse width 35 ps, repetition rate 1 Hz) with fundamental wavelength of 1064 nm were falling normally on the sample. A CW phase stabilized HeNe laser with wavelength of 632.8 nm was also made incident on the sample at the same position. Here, it should be noted that the sample behaves as a linear medium for the laser coming from the HeNe whereas Nd:YAG pulses, at a sufficient input power, can generate nonlinear photons. As a result, in transmission, we could

* romain.pierrat@espci.psl.eu

† mujumdar@tifr.res.in

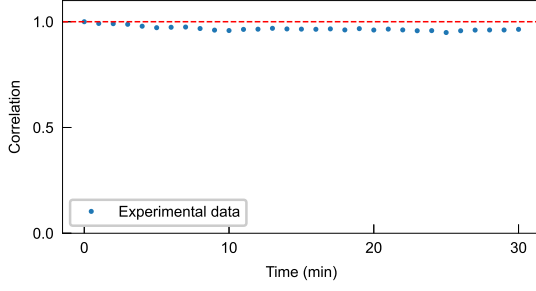


FIG. 1. Speckle correlation showing the high stability of the HeNe laser.

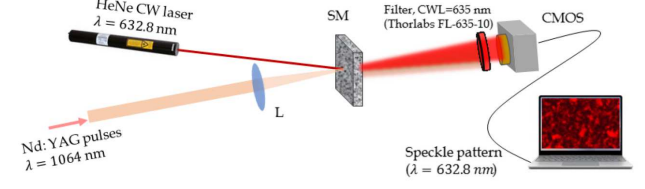


FIG. 2. Experimental setup to investigate particles' movements due to high input laser power. L: Lens, SM: Scattering medium.

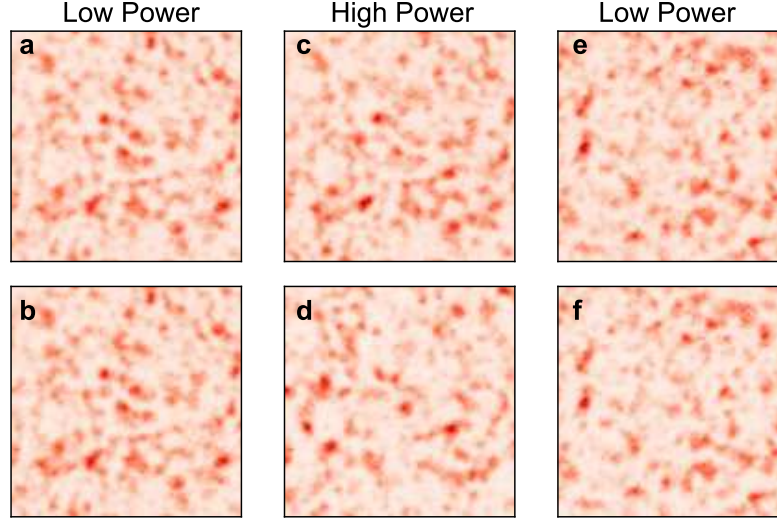


FIG. 3. Speckle patterns of red light at different scenarios. (a, b) Beginning of the experiment, power of the input pulsed laser: low. (c, d) power of the input pulsed laser: high. (e, f) Ending of the experiment, power of the input pulsed laser: low.

retrieve three speckle patterns, namely, red ($\lambda = 632.8 \text{ nm}$), IR ($\lambda = 1064 \text{ nm}$) and SH ($\lambda = 532 \text{ nm}$). For the current purpose, the speckle dynamics of the red light was monitored. A laser line filter (Thorlabs, FL-635-10) with a center wavelength of 635 nm was placed in front of a CMOS camera (Thorlabs). We captured the speckle patterns of red light while increasing the Nd:YAG laser power from very low to high and again high to low. Speckles are reported in Fig. 3 (a-f).

The first two images [(a) and (b)] correspond to consecutive Nd:YAG laser shots where the input power is very low. Clearly, the speckle patterns are almost the same over these shots. Next, we increased the input power of the Nd:YAG laser such that the second harmonic was efficiently generated. Images (c) and (d) are consecutive speckle images corresponding to this input power, and they are seen to be obviously different. This shows that the configuration of the sample was changing from shot to shot at high power. Next, we again decreased the Nd:YAG power to the minimum power and grabbed images (e) and (f) on consecutive laser pulses. Again, the speckle becomes stable when the input power reaches a very low value, since the sample is stable. Further, it is also observed that the initial [(a) and (b)] and final [(e) and (f)] red speckle patterns, although at the same low power, are completely different, which indicates that the particle configuration inside the sample has changed over the experiment. All of this clearly indicates the scatterer displacements due to the high input power.

This experiment allows us to rule out thermal effects. Thermal effects tend to work on longer timescales than impact by the radiation pressure. In the speckle pattern generated by the HeNe laser, we observed that the speckle was instantaneously reorganized when the pulse hit the sample, and immediately thereafter, the pattern was stable. There was no gradual and continuous change in the speckle for a finite time after the pulse. This motivates us to claim that, although thermal effects cannot be ruled out completely, the major contribution to the decorrelation arises from displacement due to pulse impact. Furthermore, the laser pulses were shot at too low a repetition rate to expect

a cumulative thermal effect.

II. TRANSPORT MODEL DERIVATION

This section is dedicated to the derivation of the transport model used to estimate the correlation function \mathcal{C} in the linear as well as in the second harmonic regime. This derivation is largely inspired to the standard multiple scattering theory whose details can be found in several references (see e.g. Refs. 1–3). The generalization presented here allows to take into account (1) scatterer displacements (2) second harmonic generation. Regarding the first point, the reader can also refer to Ref. 4 that presents a similar derivation. Regarding the second point, a similar approach has been used in the context of photon echoes described in Ref. 5.

A. Disorder model and scattering potential

We consider a continuous disorder model described by a fluctuating permittivity $\epsilon(\mathbf{r}, \omega)$ and a fluctuating second order nonlinear susceptibility $\chi(\mathbf{r})$. We choose to characterize their statistical properties by a Gaussian correlation function identical for both ϵ and χ since the disorder at the origin of the scattering and of second harmonic generation are the same. This gives

$$C_\epsilon(\mathbf{r}, \mathbf{r}', \omega) = \langle \delta\epsilon(\mathbf{r}, \omega) \delta\epsilon(\mathbf{r}', \omega) \rangle = |\Delta\epsilon(\omega)|^2 C(|\mathbf{r} - \mathbf{r}'|), \quad (1)$$

$$C_\chi(\mathbf{r}, \mathbf{r}') = \langle \delta\chi(\mathbf{r}) \delta\chi(\mathbf{r}') \rangle = |\Delta\chi|^2 C(|\mathbf{r} - \mathbf{r}'|), \quad (2)$$

$$\text{with } C(|\mathbf{r} - \mathbf{r}'|) = \exp \left[-\frac{|\mathbf{r} - \mathbf{r}'|^2}{2\ell^2} \right] \quad (3)$$

and where $|\Delta\epsilon(\omega)|^2$ and $|\Delta\chi|^2$ are the amplitudes and ℓ the correlation length. $\delta\epsilon(\mathbf{r}, \omega) = \epsilon(\mathbf{r}, \omega) - \langle \epsilon(\omega) \rangle$ is the fluctuating part of the permittivity. Similarly $\delta\chi(\mathbf{r}) = \chi(\mathbf{r}) - \langle \chi \rangle$ is the fluctuating part of the second order susceptibility. The disorder correlation function depends only on $|\mathbf{r} - \mathbf{r}'|$ because we consider that the disorder is statistically isotropic and homogeneous. From this model, we first define the scattering potential which is at the root of the multiple scattering theory. It is given by

$$V(\mathbf{r}, \omega) = k_0^2 [\epsilon(\mathbf{r}, \omega) - \epsilon_b(\omega)]. \quad (4)$$

ϵ_b is the background permittivity corresponding to the reference non-scattering medium. It is thus homogeneous. We now consider that there are scatterer displacements for example under the action of the radiation pressure but it can be a completely different physical process. After displacements, the new potential is given by

$$\tilde{V}(\mathbf{r}, \omega) = V(\mathbf{r} - \mathbf{\Delta}(\mathbf{r}), \omega) \quad (5)$$

where $\mathbf{\Delta}(\mathbf{r})$ is the displacement at position \mathbf{r} . In the following, we consider that this displacement is constant over a length scale of the order of ℓ . This allows to take the Fourier transform of Eq. (5) considering no position dependence in $\mathbf{\Delta}$, which gives

$$\tilde{V}(\mathbf{k}, \omega) = V(\mathbf{k}, \omega) \exp[-i\mathbf{k} \cdot \mathbf{\Delta}(\mathbf{r})]. \quad (6)$$

In a similar way, we have

$$\tilde{\chi}(\mathbf{r}) = \chi(\mathbf{r} - \mathbf{\Delta}(\mathbf{r})) \quad (7)$$

which leads to

$$\tilde{\chi}(\mathbf{k}) = \chi(\mathbf{k}) \exp[-i\mathbf{k} \cdot \mathbf{\Delta}(\mathbf{r})]. \quad (8)$$

B. Self-energy and intensity vertex

We focus now on the computation of some important building blocks regarding wave propagation in complex media that are the self-energy Σ and the intensity vertex Γ . Similarly to the scattering potential, we show how their expressions are modified in order to take into account the scatterer displacements.

We first consider the self-energy Σ and more importantly its counterpart denoted by $\tilde{\Sigma}$ when scatterer displacements are present. The self-energy is an important quantity entering the Dyson equation that drives the evolution of the statistical average electric field propagating inside a strongly scattering medium. It contains all possible scattering sequences that cannot be statistically factorized. In a dilute medium where the scattering mean-free path is large compared to the wavelength, it can be limited to the first two orders which writes

$$\Sigma(\mathbf{r}, \mathbf{r}', \omega) = \langle V(\mathbf{r}, \omega) \rangle \delta(\mathbf{r} - \mathbf{r}') + \langle V(\mathbf{r}, \omega) G_b(\mathbf{r} - \mathbf{r}', \omega) V(\mathbf{r}', \omega) \rangle_c \quad (9)$$

where $\langle \cdot \rangle_c$ represents a statistical average restricted to the connected part, i.e. $\langle V G_b V \rangle_c = \langle V G_b V \rangle - \langle V \rangle G_b \langle V \rangle$. G_b is the Green function in the reference medium, it describes the field propagation between two consecutive scattering events on the potential V . For the case of scatterer displacements, we have

$$\tilde{\Sigma}(\mathbf{r}, \mathbf{r}', \omega) = \left\langle \tilde{V}(\mathbf{r}, \omega) \right\rangle \delta(\mathbf{r} - \mathbf{r}') + \left\langle \tilde{V}(\mathbf{r}, \omega) G_b(\mathbf{r} - \mathbf{r}', \omega) \tilde{V}(\mathbf{r}', \omega) \right\rangle_c. \quad (10)$$

It is important to keep in mind that the statistical average performed here is not only an average over all possible configurations of the disorder but is also an average over the displacements. By Fourier transforming Eqs. (10) and (9) and using Eq. (6), we obtain

$$\tilde{\Sigma}(\mathbf{k}, \mathbf{k}', \omega) = \Sigma(\mathbf{k}, \mathbf{k}', \omega) \int \exp[-i(\mathbf{k} - \mathbf{k}') \cdot \mathbf{\Delta}] f(\mathbf{r}, \mathbf{\Delta}) d\mathbf{\Delta} \quad (11)$$

where $f(\mathbf{r}, \mathbf{\Delta})$ is the probability density to have a displacement $\mathbf{\Delta}$ at position \mathbf{r} . From the statistical homogeneity and isotropy of the disorder, we get

$$\Sigma(\mathbf{k}, \mathbf{k}', \omega) = 8\pi^3 \delta(\mathbf{k} - \mathbf{k}') \check{\Sigma}(k, \omega) \quad \text{and} \quad \tilde{\Sigma}(\mathbf{k}, \mathbf{k}', \omega) = 8\pi^3 \delta(\mathbf{k} - \mathbf{k}') \check{\check{\Sigma}}(k, \omega) \quad (12)$$

which leads to

$$\check{\check{\Sigma}}(k, \omega) = \check{\Sigma}(k, \omega) \quad (13)$$

where $\check{\Sigma}$ and $\check{\check{\Sigma}}$ are the reduced self-energies. Since the extinction mean-free path is given by the imaginary part of the reduced self-energy, we have

$$\frac{1}{\ell_e(\omega)} = \frac{\text{Im } \check{\Sigma}(k_0, \omega)}{k_0} = \frac{\text{Im } \check{\check{\Sigma}}(k_0, \omega)}{k_0} = \frac{1}{\bar{\ell}_e(\omega)}. \quad (14)$$

By invoking the non-absorbing nature of the medium we finally get equality between the scattering mean-free paths with and without scatterer displacements. Inserting the expression of the correlation function C_ϵ into Eq. (9) leads to

$$\frac{1}{\bar{\ell}_s(\omega)} = \frac{1}{\ell_s(\omega)} = \frac{k_0^4 |\Delta\epsilon(\omega)|^2}{16\pi^2} \int C(q) d\Omega \quad (15)$$

where $q = 2k_0 \sin(\theta/2)$ is the modulus of the scattering vector and $d\Omega = \sin\theta d\theta d\phi$ is the elementary solid angle in standard spherical units. From Eq. (3), we get

$$C(q) = \int \exp\left[-\frac{\mathbf{R}^2}{2\ell^2} - i\mathbf{q} \cdot \mathbf{R}\right] d\mathbf{R} = \ell^3 (2\pi)^{3/2} \exp\left[-\frac{q^2 \ell^2}{2}\right] \quad (16)$$

which finally gives

$$\frac{1}{\bar{\ell}_s(\omega)} = \frac{1}{\ell_s(\omega)} = k_0^2 \ell |\Delta\epsilon(\omega)|^2 \frac{\sqrt{2\pi}}{4} [1 - \exp(-2k_0^2 \ell^2)]. \quad (17)$$

The same analysis has now to be applied to the intensity vertex Γ and its counterpart $\tilde{\Gamma}$ when scatterer displacements are present. The intensity vertex is an important quantity entering the Bethe-Salpeter equation that describes the evolution of the field-field correlation function. It contains all possible scattering sequences for the field and its complex conjugate counterpart that cannot be statistically factorized. Still in a dilute medium, it can be limited to the first order which writes

$$\Gamma(\mathbf{r}, \mathbf{r}', \boldsymbol{\rho}, \boldsymbol{\rho}', \omega) = \langle V(\mathbf{r}, \omega) V^*(\boldsymbol{\rho}, \omega) \rangle_c \delta(\mathbf{r}' - \mathbf{r}) \delta(\boldsymbol{\rho}' - \boldsymbol{\rho}). \quad (18)$$

For the case of scatterer displacements, we have

$$\tilde{\Gamma}(\mathbf{r}, \mathbf{r}', \boldsymbol{\rho}, \boldsymbol{\rho}', \omega) = \left\langle V(\mathbf{r}, \omega) \tilde{V}^*(\boldsymbol{\rho}, \omega) \right\rangle_c \delta(\mathbf{r}' - \mathbf{r}) \delta(\boldsymbol{\rho} - \boldsymbol{\rho}'). \quad (19)$$

It is important to note that the correlation \mathcal{C} involves the electric field before any displacement (E) and its complex conjugate counterpart after displacement (\tilde{E}^*). This is the reason why only the complex conjugated potential is replaced in Eq. (19) compared to Eq. (18). We also note that although the potential is real, we keep the complex conjugate notation for the sake of understanding, i.e. to show that it applies to the complex conjugate field. By Fourier transforming Eqs. (19) and (18) and using Eqs. (6), we obtain

$$\tilde{\Gamma}(\mathbf{k}, \mathbf{k}', \boldsymbol{\kappa}, \boldsymbol{\kappa}', \omega) = \Gamma(\mathbf{k}, \mathbf{k}', \boldsymbol{\kappa}, \boldsymbol{\kappa}', \omega) \int \exp[-i(\boldsymbol{\kappa} - \boldsymbol{\kappa}') \cdot \boldsymbol{\Delta}] f(\mathbf{r}, \boldsymbol{\Delta}) d\boldsymbol{\Delta}. \quad (20)$$

From the statistical homogeneity of the disorder, we get

$$\check{\Gamma}(\mathbf{k}, \mathbf{k}', \boldsymbol{\kappa}, \boldsymbol{\kappa}', \omega) = 8\pi^3 \delta(\mathbf{k} - \mathbf{k}' - \boldsymbol{\kappa} + \boldsymbol{\kappa}') \Gamma(\mathbf{k}, \mathbf{k}', \boldsymbol{\kappa}, \boldsymbol{\kappa}', \omega), \quad (21)$$

$$\check{\check{\Gamma}}(\mathbf{k}, \mathbf{k}', \boldsymbol{\kappa}, \boldsymbol{\kappa}', \omega) = 8\pi^3 \delta(\mathbf{k} - \mathbf{k}' - \boldsymbol{\kappa} + \boldsymbol{\kappa}') \check{\Gamma}(\mathbf{k}, \mathbf{k}', \boldsymbol{\kappa}, \boldsymbol{\kappa}', \omega), \quad (22)$$

which finally leads to

$$\check{\check{\Gamma}}(\mathbf{k}, \mathbf{k}', \boldsymbol{\kappa}, \boldsymbol{\kappa}', \omega) = \check{\Gamma}(\mathbf{k}, \mathbf{k}', \boldsymbol{\kappa}, \boldsymbol{\kappa}', \omega) \int \exp[-i(\boldsymbol{\kappa} - \boldsymbol{\kappa}') \cdot \boldsymbol{\Delta}] f(\mathbf{r}, \boldsymbol{\Delta}) d\boldsymbol{\Delta} \quad (23)$$

where $\check{\Gamma}$ and $\check{\check{\Gamma}}$ are the reduced intensity vertices. The standard phase function is given by $\check{\Gamma}$ through the relation

$$\frac{1}{\ell_s(\omega)} p(\mathbf{u}, \mathbf{u}', \omega) = \frac{1}{16\pi^2} \check{\Gamma}(k_0 \mathbf{u}, k_0 \mathbf{u}', k_0 \mathbf{u}, k_0 \mathbf{u}', \omega). \quad (24)$$

By definition, the phase function p is normalized such that

$$\int p(\mathbf{u}, \mathbf{u}', \omega) d\Omega' = 1. \quad (25)$$

These results allow to define a generalized phase function \tilde{p} for the case where there are scatterer displacements given by

$$\frac{1}{\ell_s(\omega)} \tilde{p}(\mathbf{r}, \mathbf{u}, \mathbf{u}', \omega) = \frac{1}{\ell_s(\omega)} p(\mathbf{u}, \mathbf{u}', \omega) g(\mathbf{r}, \mathbf{u}, \mathbf{u}', \omega) = \frac{1}{16\pi^2} \check{\check{\Gamma}}(k_0 \mathbf{u}, k_0 \mathbf{u}', k_0 \mathbf{u}, k_0 \mathbf{u}', \omega) \quad (26)$$

where

$$g(\mathbf{r}, \mathbf{u}, \mathbf{u}', \omega) = \int \exp[-i\mathbf{q} \cdot \boldsymbol{\Delta}] f(\mathbf{r}, \boldsymbol{\Delta}) d\boldsymbol{\Delta} \quad (27)$$

and $\mathbf{q} = k_0(\mathbf{u} - \mathbf{u}')$ is the scattering vector. Plugging the expression of the correlation function C_ϵ into Eq. (18) leads to

$$p(\mathbf{u}, \mathbf{u}', \omega) = \frac{k_0^2 \ell^2 \exp[-q^2 \ell^2 / 2]}{2\pi [1 - \exp(-2k_0^2 \ell^2)]}. \quad (28)$$

This concludes the computation of the building blocks required to describe light propagation in a diluted dynamic scattering medium.

C. Linear regime

We now consider the case of light transport in the linear regime. In a dilute medium such that $k_0 \ell_s \gg 1$, we can show that the field and its complex conjugate follow the same scattering sequences (after statistical average) which can be represented by the following diagram:

$$\begin{array}{c} E(\mathbf{r}, \omega) \text{---} \bigcirc \text{---} \bigcirc \text{---} \bigcirc \text{---} E_0 \\ | \quad | \quad | \\ \tilde{E}^*(\mathbf{r}, \omega) \text{---} \bigcirc \text{---} \bigcirc \text{---} \bigcirc \text{---} E_0^* \end{array} \quad (29)$$

In this representation, the top line represents a path for the electric field E and the bottom line is for a path of its complex conjugate \tilde{E}^* in presence of scatterer displacements. Solid and dashed thick lines correspond to average Green functions (describing propagation between consecutive scattering events) and average fields respectively. Circles denote scattering events and vertical dashed lines represent statistical correlations between scattering events through Eq. (2).

This specific diagram is called the ladder and is the leading contribution to the expression of the field-field correlation function \mathcal{C} . Indeed the fact that it corresponds to the same path for the field and its complex conjugate implies that there is always constructive interference between both. From this diagram, we deduce that the correlation function \mathcal{C} is described by a Radiative Transfer Equation (RTE) which writes [1]

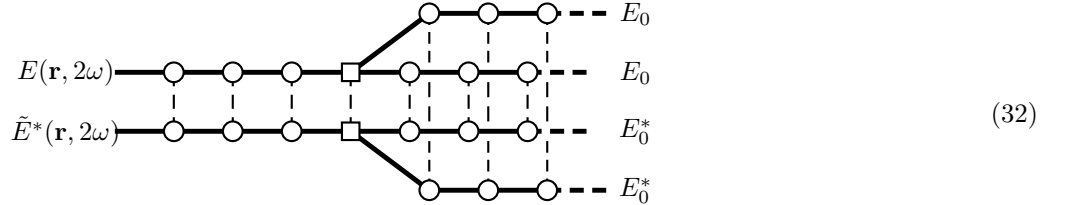
$$\left[\mathbf{u} \cdot \nabla_{\mathbf{r}} + \frac{1}{\ell_s(\omega)} \right] \tilde{I}(\mathbf{r}, \mathbf{u}, \omega) = \frac{1}{\ell_s(\omega)} \int p(\mathbf{u}, \mathbf{u}', \omega) g(\mathbf{r}, \mathbf{u}, \mathbf{u}', \omega) \tilde{I}(\mathbf{r}, \mathbf{u}', \omega) d\mathbf{u}' \quad (30)$$

where the specific intensity \tilde{I} is defined by the field-field correlation

$$\delta(k - k_0) \tilde{I}(\mathbf{r}, \mathbf{u}, \omega) = \int \left\langle E\left(\mathbf{r} + \frac{\mathbf{s}}{2}, \omega\right) \tilde{E}^*\left(\mathbf{r} - \frac{\mathbf{s}}{2}, \omega\right) \right\rangle e^{-ik\mathbf{u} \cdot \mathbf{s}} d\mathbf{s}. \quad (31)$$

D. Second harmonic regime

We now move on to the second harmonic regime. As stated in the main text, we apply a perturbative approach to compute the second harmonic correlation. This means that we have first the propagation of the field at the frequency ω , then second harmonic generation and finally propagation of the field at the frequency 2ω . That being said, the most difficult task now is to determine the typical pairs of paths for the field and its complex conjugate that have the leading contribution to the correlation. This is equivalent to determine the diagrams that lead to constructive interferences. We follow the same idea than for the linear regime thus assuming that we have essentially ladder diagrams for the beams at ω and 2ω . However these ladders have to be connected by a kernel corresponding to the second harmonic generation process. This leads to the diagram



where the squares denote the second harmonic processes. We may consider that the non-linear processes occur at two different positions for the electric field E and its complex conjugate counterpart \tilde{E}^* . However, this would lead to a propagation of the correlations $\langle E(\mathbf{r}, \omega) \tilde{E}^*(\mathbf{r}, 2\omega) \rangle$ or $\langle E(\mathbf{r}, 2\omega) \tilde{E}^*(\mathbf{r}, \omega) \rangle$ which are supposed to vanish since they involve fields at two different frequencies. This is the reason why we have a disorder correlation function C_ϵ between the second harmonic processes (dashed line between the squares). Strictly speaking, we should also take into account the degeneracy of the diagram (factor 4). Indeed, it corresponds to all possible permutations of the incident fields. However, this will not play any role in the following and this factor will be taken into account in the constant α .

The kernel dressed with the two ladders at frequency ω can be considered as a source term for the second harmonic ladder. It is given by

$$S(\mathbf{r}, \boldsymbol{\rho}, 2\omega) = \int \langle G(\mathbf{r} - \mathbf{r}', 2\omega) \rangle \langle G^*(\boldsymbol{\rho} - \boldsymbol{\rho}', 2\omega) \rangle \tilde{\Gamma}_{\text{SHG}}(\mathbf{r}', \mathbf{r}'', \mathbf{r}''', \boldsymbol{\rho}', \boldsymbol{\rho}'', \boldsymbol{\rho}''', 2\omega) \\ \times \langle E(\mathbf{r}'', \omega) \tilde{E}^*(\boldsymbol{\rho}'', 2\omega) \rangle \langle E(\mathbf{r}''', \omega) \tilde{E}^*(\boldsymbol{\rho}''', 2\omega) \rangle d\mathbf{r}' d\mathbf{r}'' d\mathbf{r}''' d\boldsymbol{\rho}' d\boldsymbol{\rho}'' d\boldsymbol{\rho}''' \quad (33)$$

where $\tilde{\Gamma}_{\text{SHG}}$ is the SHG vertex given by

$$\tilde{\Gamma}_{\text{SHG}}(\mathbf{r}, \mathbf{r}', \mathbf{r}'', \boldsymbol{\rho}, \boldsymbol{\rho}', \boldsymbol{\rho}'', \omega) = \langle \chi(\mathbf{r}) \tilde{\chi}^*(\boldsymbol{\rho}) \rangle_c \delta(\mathbf{r} - \mathbf{r}') \delta(\mathbf{r} - \mathbf{r}'') \delta(\boldsymbol{\rho} - \boldsymbol{\rho}') \delta(\boldsymbol{\rho} - \boldsymbol{\rho}''). \quad (34)$$

Similarly to the case of $\tilde{\Gamma}$, we keep the complex conjugate notation for the second order susceptibility although it is a real quantity in order remind that it corresponds to the complex conjugate field. Without any scatterer displacement, we have

$$\Gamma_{\text{SHG}}(\mathbf{r}, \mathbf{r}', \mathbf{r}'', \boldsymbol{\rho}, \boldsymbol{\rho}', \boldsymbol{\rho}'', \omega) = \langle \chi(\mathbf{r}) \tilde{\chi}^*(\boldsymbol{\rho}) \rangle_c \delta(\mathbf{r} - \mathbf{r}') \delta(\mathbf{r} - \mathbf{r}'') \delta(\boldsymbol{\rho} - \boldsymbol{\rho}') \delta(\boldsymbol{\rho} - \boldsymbol{\rho}''). \quad (35)$$

By Fourier transforming Eqs. (34) and (35) and making use of Eq. (8), we obtain

$$\tilde{\Gamma}_{\text{SHG}}(\mathbf{k}, \mathbf{k}', \mathbf{k}'', \boldsymbol{\kappa}, \boldsymbol{\kappa}', \boldsymbol{\kappa}'', \omega) = \Gamma_{\text{SHG}}(\mathbf{k}, \mathbf{k}', \mathbf{k}'', \boldsymbol{\kappa}, \boldsymbol{\kappa}', \boldsymbol{\kappa}'', \omega) \int \exp[-i(\boldsymbol{\kappa} - \boldsymbol{\kappa}' - \boldsymbol{\kappa}'') \cdot \boldsymbol{\Delta}] f(\mathbf{r}, \boldsymbol{\Delta}) d\boldsymbol{\Delta}. \quad (36)$$

From the statistical homogeneity of the disorder, we get

$$\check{\Gamma}_{\text{SHG}}(\mathbf{k}, \mathbf{k}', \mathbf{k}'', \boldsymbol{\kappa}, \boldsymbol{\kappa}', \boldsymbol{\kappa}'', \omega) = 8\pi^3 \delta(\mathbf{k} - \mathbf{k}' - \mathbf{k}'' - \boldsymbol{\kappa} + \boldsymbol{\kappa}' + \boldsymbol{\kappa}'') \Gamma_{\text{SHG}}(\mathbf{k}, \mathbf{k}', \mathbf{k}'', \boldsymbol{\kappa}, \boldsymbol{\kappa}', \boldsymbol{\kappa}'', \omega), \quad (37)$$

$$\check{\check{\Gamma}}_{\text{SHG}}(\mathbf{k}, \mathbf{k}', \mathbf{k}'', \boldsymbol{\kappa}, \boldsymbol{\kappa}', \boldsymbol{\kappa}'', \omega) = 8\pi^3 \delta(\mathbf{k} - \mathbf{k}' - \mathbf{k}'' - \boldsymbol{\kappa} + \boldsymbol{\kappa}' + \boldsymbol{\kappa}'') \check{\Gamma}_{\text{SHG}}(\mathbf{k}, \mathbf{k}', \mathbf{k}'', \boldsymbol{\kappa}, \boldsymbol{\kappa}', \boldsymbol{\kappa}'', \omega), \quad (38)$$

which finally leads to

$$\check{\check{\Gamma}}_{\text{SHG}}(\mathbf{k}, \mathbf{k}', \mathbf{k}'', \boldsymbol{\kappa}, \boldsymbol{\kappa}', \boldsymbol{\kappa}'', \omega) = \check{\Gamma}_{\text{SHG}}(\mathbf{k}, \mathbf{k}', \mathbf{k}'', \boldsymbol{\kappa}, \boldsymbol{\kappa}', \boldsymbol{\kappa}'', \omega) \int \exp[-i(\boldsymbol{\kappa} - \boldsymbol{\kappa}' - \boldsymbol{\kappa}'') \cdot \boldsymbol{\Delta}] f(\mathbf{r}, \boldsymbol{\Delta}) d\boldsymbol{\Delta} \quad (39)$$

where $\check{\Gamma}_{\text{SHG}}$ and $\check{\check{\Gamma}}_{\text{SHG}}$ are the reduced SHG vertices. From this, we can define a SHG phase function given by

$$\alpha p_{\text{SHG}}(\mathbf{u}, \mathbf{u}', \mathbf{u}'', \omega) = \frac{1}{125\pi^5} \check{\Gamma}_{\text{SHG}}(2k_0\mathbf{u}, k_0\mathbf{u}', k_0\mathbf{u}'', 2k_0\mathbf{u}, k_0\mathbf{u}', k_0\mathbf{u}'', \omega). \quad (40)$$

α is a coefficient that takes into account all constants involved in the second harmonic process and is such that the second harmonic phase function is normalized, i.e.

$$\int p_{\text{SHG}}(\mathbf{u}, \mathbf{u}', \mathbf{u}'', \omega) d\Omega' d\Omega'' = 1. \quad (41)$$

These results allow to define a generalized SHG phase function given by

$$\alpha \tilde{p}_{\text{SHG}}(\mathbf{u}, \mathbf{u}', \mathbf{u}'', \omega) = \alpha p_{\text{SHG}}(\mathbf{u}, \mathbf{u}', \mathbf{u}'', \omega) g_{\text{SHG}}(\mathbf{r}, \mathbf{u}, \mathbf{u}', \mathbf{u}'', \omega) = \frac{1}{125\pi^5} \check{\Gamma}_{\text{SHG}}(2k_0\mathbf{u}, k_0\mathbf{u}', k_0\mathbf{u}'', 2k_0\mathbf{u}, k_0\mathbf{u}', k_0\mathbf{u}'', \omega) \quad (42)$$

where

$$g_{\text{SHG}}(\mathbf{r}, \mathbf{u}, \mathbf{u}', \mathbf{u}'', \omega) = \int \exp[-i\mathbf{q} \cdot \boldsymbol{\Delta}] f(\mathbf{r}, \boldsymbol{\Delta}) d\boldsymbol{\Delta} \quad (43)$$

with $\mathbf{q} = k_0(2\mathbf{u} - \mathbf{u}' - \mathbf{u}'')$ the SHG scattering vector. Plugging the expression of the correlation function C_χ into Eq. (35) leads to

$$p_{\text{SHG}}(\mathbf{u}, \mathbf{u}', \mathbf{u}'', \omega) \propto \exp\left[-\frac{q^2 \ell^2}{2}\right]. \quad (44)$$

We finally get the formulation of the RTE for the second harmonic specific intensity linked to the second harmonic correlation function which reads

$$\left[\mathbf{u} \cdot \nabla_{\mathbf{r}} + \frac{1}{\ell_s(2\omega)}\right] \tilde{I}(\mathbf{r}, \mathbf{u}, 2\omega) = \frac{1}{\ell_s(2\omega)} \int p(\mathbf{u} \cdot \mathbf{u}', 2\omega) g(\mathbf{u} \cdot \mathbf{u}', 2\omega) \tilde{I}(\mathbf{r}, \mathbf{u}', 2\omega) d\mathbf{u}' \\ + \alpha \iint p_{\text{SHG}}(\mathbf{u}, \mathbf{u}', \mathbf{u}'', \omega) g_{\text{SHG}}(\mathbf{u}, \mathbf{u}', \mathbf{u}'', \omega) \tilde{I}(\mathbf{r}, \mathbf{u}', \omega) \tilde{I}(\mathbf{r}, \mathbf{u}'', \omega) d\mathbf{u}' d\mathbf{u}''. \quad (45)$$

The second harmonic specific intensity is still given by the field-field correlation

$$\delta(k - k_0) \tilde{I}(\mathbf{r}, \mathbf{u}, 2\omega) = \int \left\langle E\left(\mathbf{r} + \frac{\mathbf{s}}{2}, 2\omega\right) \tilde{E}^*\left(\mathbf{r} - \frac{\mathbf{s}}{2}, 2\omega\right) \right\rangle e^{-ik\mathbf{u} \cdot \mathbf{s}} d\mathbf{s}. \quad (46)$$

This concludes the derivation of the RTE for the linear and second harmonic beams.

III. VALIDITY CHECK FROM AB INITIO SIMULATIONS

The model developed in the previous section has been obtained under several approximations. The most important one concerns the diagrams that have to be taken into account in order to estimate the second harmonic specific intensity. In a dilute medium, we have considered that a ladder-type diagram is the leading contribution to the second harmonic speckle correlation. In order to check the validity of this approximation, we have run *ab initio* simulations of Maxwell equations using a coupled-dipole formalism and compared the results to the RTE model solved using a Monte Carlo scheme.

It is important to note that we consider here a simplified model that does not reflect the conditions of the experiment but it will help to check the validity of the transport model. In particular, the coupled-dipole formalism used here implies that the disorder model is limited to point scatterers randomly located inside the medium. Regarding the scatterer displacement model, we simply consider that a scatterer can move in an arbitrary direction over a distance d that is fixed.

Moreover the numerical resolution of Maxwell equations requires significant computing resources. This is the reason why we restrict to 2D systems in TE polarization (electric field along the direction of invariance by translation). This means that a scalar model can be used and no polarization effects have to be taken into account.

A. Coupled-dipole model

1. Linear regime

In the linear regime, the coupled-dipole equations are given by

$$E_i(\omega) = E_0(\mathbf{r}_i, \omega) + k_0^2 \alpha(\omega) \sum_{\substack{j=1 \\ j \neq i}}^N G_0(\mathbf{r}_i - \mathbf{r}_j, \omega) E_j(\omega), \quad (47)$$

$$E(\mathbf{r}, \omega) = E_0(\mathbf{r}, \omega) + k_0^2 \alpha(\omega) \sum_{j=1}^N G_0(\mathbf{r} - \mathbf{r}_j, \omega) E_j(\omega). \quad (48)$$

E_i represents the field illuminating the scatterer i lying at position \mathbf{r}_i . It is also called the exciting field. It is given by two contributions: the incident field E_0 and the field scattered by all other scatterers. $G_0(\mathbf{r} - \mathbf{r}_0, \omega)$ is the Green function in vacuum. It links the field created at position \mathbf{r} by a source dipole $p(\omega)$ lying at position \mathbf{r}_0 through the relation

$$E(\mathbf{r}, \omega) = \mu_0 \omega^2 G_0(\mathbf{r} - \mathbf{r}_0, \omega) p(\omega). \quad (49)$$

For 2D TE waves, it is given by

$$G_0(\mathbf{R}, \omega) = \frac{i}{4} H_0^{(1)}(k_0 |\mathbf{R}|) \quad (50)$$

where $H_0^{(1)}$ is the Hankel function of first kind and zero order. $\alpha(\omega)$ is the polarizability of the scatterer. It describes the optical response of the particle. In the non-absorbing case, energy conservation implies

$$k_0 \text{Im} \alpha(\omega) = \frac{k_0^3}{4} |\alpha(\omega)|^2. \quad (51)$$

Once the exciting fields have been computed for all dipoles by solving the set of Eqs. (47), the field at any position, i.e. $E(\mathbf{r}, \omega)$, can be computed using Eq. (48).

In order to take into account scatterer displacements, we just have to redo the same computation after moving the scatterers by a distance d in arbitrary directions. Then we have access to $\tilde{E}(\mathbf{r}, \omega)$. An average over several disorder configurations allows to estimate the correlation function

$$c_{\text{CD}}(\mathbf{r}, \omega) = \frac{\langle E(\mathbf{r}, \omega) \tilde{E}^*(\mathbf{r}, \omega) \rangle}{\langle E(\mathbf{r}, \omega) E^*(\mathbf{r}, \omega) \rangle} \quad (52)$$

where the subscript CD means ‘‘Coupled Dipoles’’.

2. Non-linear regime

The second harmonic regime is still considered through the standard perturbative approach. This means that the coupled-dipole equations write

$$E_i(2\omega) = \frac{\beta}{\alpha(2\omega)} E_i(\omega)^2 + k_0^2 \alpha(2\omega) \sum_{\substack{j=1 \\ j \neq i}}^N G_0(\mathbf{r}_i - \mathbf{r}_j, 2\omega) E_j(2\omega), \quad (53)$$

$$E(\mathbf{r}, 2\omega) = k_0^2 \alpha(2\omega) \sum_{j=1}^N G_0(\mathbf{r} - \mathbf{r}_j, 2\omega) E_j(2\omega) \quad (54)$$

where β can be seen as a second harmonic polarizability. This set of equations is solved using the results of the linear case and following exactly the same steps. This leads to an estimate of the correlation function

$$C_{CD}(\mathbf{r}, 2\omega) = \frac{\langle E(\mathbf{r}, 2\omega) \tilde{E}^*(\mathbf{r}, 2\omega) \rangle}{\langle E(\mathbf{r}, 2\omega) E^*(\mathbf{r}, 2\omega) \rangle}. \quad (55)$$

B. Monte Carlo scheme

In order to solve the set of transport equations, we have performed Monte Carlo simulations. For a cloud of uncorrelated point dipoles lying in a 2D dilute medium and considering TE waves, the parameters are given by

$$\ell_s(\omega) = \frac{1}{\rho \sigma_s(\omega)} \quad \text{where} \quad \sigma_s(\omega) = \frac{k_0^3}{4} |\alpha(\omega)|^2, \quad (56)$$

$$p(\mathbf{u}, \mathbf{u}', \omega) = \frac{1}{2\pi}, \quad p_{SHG}(\mathbf{u}, \mathbf{u}', \mathbf{u}'', \omega) = \frac{1}{4\pi^2} \quad (57)$$

$$\text{and} \quad f(\mathbf{r}, \Delta) = \frac{\delta(\Delta - d)}{2\pi\Delta}, \quad (58)$$

ρ being the density of scatterers. Two different Monte Carlo simulations are done. The first one solves Eq. (30). This is a fully standard Monte Carlo scheme except that we have to multiply the energy quanta of the random walk packets by $g(\mathbf{r}, \mathbf{u}, \mathbf{u}', \omega)$ at each scattering event in order to take into account the decorrelation process. At the end, we have access to a map of the specific intensity $\tilde{I}(\mathbf{r}, \mathbf{u}, \omega)$ which is used to compute the correlation function

$$C_{MC}(\mathbf{r}, \omega) = \frac{\int \tilde{I}(\mathbf{r}, \mathbf{u}, \omega) d\mathbf{u}}{\int I(\mathbf{r}, \mathbf{u}, \omega) d\mathbf{u}} \quad (59)$$

where the subscript MC means ‘‘Monte Carlo’’. The second Monte Carlo simulation is used to solve Eq. (45) and is similar to the first one except that the source term is given by the SHG process [last term of Eq. (45)]. At the end, we have access to the specific intensity $\tilde{I}(\mathbf{r}, \mathbf{u}, 2\omega)$ which gives the correlation function

$$C_{MC}(\mathbf{r}, 2\omega) = \frac{\int \tilde{I}(\mathbf{r}, \mathbf{u}, 2\omega) d\mathbf{u}}{\int I(\mathbf{r}, \mathbf{u}, 2\omega) d\mathbf{u}}. \quad (60)$$

C. Numerical result comparison

To make comparisons between the couple-dipole formalism and the Monte carlo simulations, we consider a slab geometry of thickness L illuminated by a plane-wave at normal incidence as represented in Fig. 4(b). However this very simple model have to be slightly adapted in the case of the coupled-dipole simulation which is detailed in Fig. 4(a). Indeed, the finite number of scatterers imposes a finite transverse size D . Moreover, in order to avoid diffraction effects at the transverse boundaries, we choose to illuminate the medium by a gaussian beam of waist w . We choose $D \gg \{L, w\}$ and $w \gg \{L, \lambda\}$. The speckle correlation functions are computed just behind the slab, at a distance r from the interface and average along a transverse distance a in the case of the coupled dipole simulation. In the case of the Monte Carlo simulation, we consider the full transmitted specific intensity.

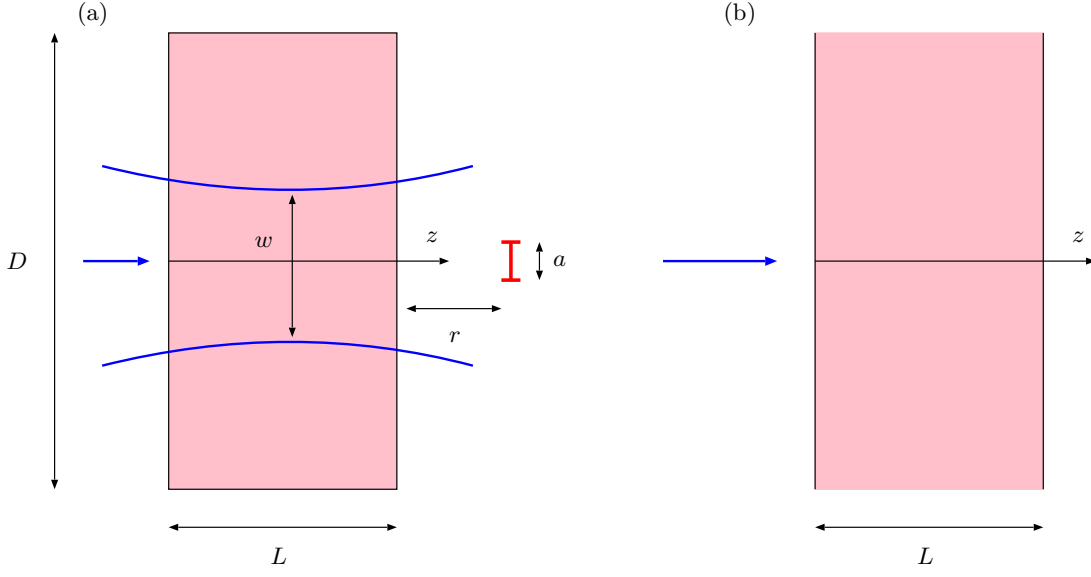


FIG. 4. 2D slab geometry considered to validate the transport approach. (a) Scattering rectangle used in the coupled-dipole simulation. We have $D \gg \{L, w\}$ and $w \gg \{L, \lambda\}$ to mimic a slab geometry shine with a plane-wave at normal incidence. a is the transverse size of the detection zone where we compute the correlation functions \mathcal{C} . We have $w \gg a \gg \lambda$ to capture several speckle grains in order to improve the statistical convergence. We have also $r > \lambda$ to avoid near-field interaction close to the interface. (b) Infinite scattering slab used in the Monte Carlo simulation. Since the *ab initio* computation is done using point dipoles, the standard phase function p as well as the SHG phase function p_{SHG} are chosen to be isotropic ($g = 0$).

We have tested several sets of parameters, each of them giving rise to a very good agreement between the results of both numerical approaches. This proves that the theoretical model is accurate and that the diagram considered for the second harmonic correlation function is the leading term. As an example, we show in Fig. 5 the results for an optical thickness $b = L/\ell_s = 2$ for both the linear and second harmonic beams.

IV. DIFFUSION LIMIT

This section is dedicated to obtaining analytical expressions of the correlation functions in the diffusion limit. We consider a 3D slab geometry of thickness L illuminated by a plane-wave at normal incidence. This implies that all physical quantities will depend only on the depth z inside the medium. The diffusion approximation requires that $L \gg \{\ell_t(\omega), \ell_t(2\omega)\}$, ℓ_t being the transport mean-free path. We also assume that the displacement direction of the scatterers is isotropic which leads to

$$f(\mathbf{r}, \Delta) = \frac{f(\Delta)}{4\pi\Delta^2}. \quad (61)$$

A. Linear regime

We first consider the linear regime. Defining the absorption length $\tilde{\ell}_a$ and the anisotropy factor \tilde{g} by

$$\frac{1}{\tilde{\ell}_a(\omega)} = \frac{1}{\ell_e(\omega)} - \frac{1}{\tilde{\ell}_s(\omega)} = \frac{1}{\ell_s(\omega)} \left[1 - \int p(\mathbf{u} \cdot \mathbf{u}', \omega) g(\mathbf{u} \cdot \mathbf{u}', \omega) d\mathbf{u}' \right], \quad (62)$$

$$\tilde{g}(\omega) = \frac{1}{\tilde{\ell}_s(\omega)} \int \tilde{p}(\mathbf{u} \cdot \mathbf{u}', \omega) \mathbf{u} \cdot \mathbf{u}' d\mathbf{u}' = \frac{\int p(\mathbf{u} \cdot \mathbf{u}', \omega) g(\mathbf{u} \cdot \mathbf{u}', \omega) \mathbf{u} \cdot \mathbf{u}' d\mathbf{u}'}{\int p(\mathbf{u} \cdot \mathbf{u}', \omega) g(\mathbf{u} \cdot \mathbf{u}', \omega) d\mathbf{u}'}, \quad (63)$$

we are back to the standard RTE with an absorption term. Thus we can apply the no less standard diffusion equation derivation in the framework of the P1-approximation [6]. Since the diffusion equation is valid only for the diffuse part of the correlation function, we split it into its ballistic (C_b) and diffuse (C_d) components which gives

$$C(\mathbf{r}, \omega) = \langle E(\mathbf{r}, \omega) \rangle \langle \tilde{E}^*(\mathbf{r}, \omega) \rangle + \langle \delta E(\mathbf{r}, \omega) \delta \tilde{E}^*(\mathbf{r}, \omega) \rangle = C_b(\mathbf{r}, \omega) + C_d(\mathbf{r}, \omega). \quad (64)$$

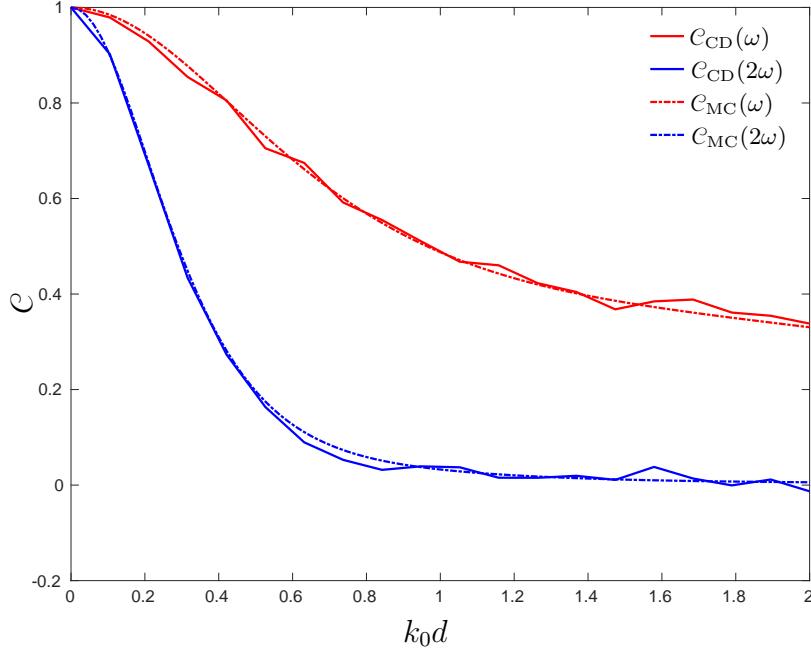


FIG. 5. Comparison of the correlation functions obtained using the coupled dipole simulations (C_{CD}) and the Monte Carlo schemes (C_{MC}) for the linear (ω) and second harmonic (2ω) beams as a function of the normalized displacement distance $k_0 d$. The parameters are $k_0 L = 100$, $k_0 D = 8000$, $k_0/\sqrt{\rho} = 6$, $k_0 w = 3800$, $k_0 r = 5$ and $k_0 a = 8$. The polarizability is chosen such that $k_0 \ell_s(\omega) = 50$ and $k_0 \ell_s(2\omega) = 50$ which leads to $b(\omega) = b(2\omega) = 2$. $N_c = 256$ configurations are used for the coupled dipole simulations and $N_p = 5 \times 10^6$ random walk packets are used for the Monte Carlo schemes.

This splitting is similar to the one we perform usually on the average intensity. The ballistic component is given by

$$C_b(z, \omega) = I_0 \exp[-z/\ell_s(\omega)] \quad (65)$$

and its diffuse counterpart reads

$$\left[-\frac{\tilde{\ell}_s(\omega)\tilde{\ell}_t(\omega)}{3} \frac{\partial^2}{\partial z^2} + \frac{\tilde{\ell}_s(\omega)}{\tilde{\ell}_a(\omega)} \right] C_d(z, \omega) = \frac{1}{1 - \tilde{g}(\omega)} C_b(z, \omega) \quad (66)$$

where the transport mean-free path is given by

$$\tilde{\ell}_t(\omega) = \frac{\tilde{\ell}_s(\omega)}{1 - \tilde{g}(\omega)}. \quad (67)$$

The boundary conditions involve the standard extrapolation length $\tilde{z}_0(\omega) = 2\tilde{\ell}_t(\omega)/3$ and are given by

$$C_d(z = 0, \omega) - \tilde{z}_0(\omega) \frac{\partial C_d}{\partial z}(z = 0, \omega) = -\frac{2\tilde{g}(\omega)}{1 - \tilde{g}(\omega)} C_b(z = 0, \omega), \quad (68)$$

$$C_d(z = L, \omega) + \tilde{z}_0(\omega) \frac{\partial C_d}{\partial z}(z = L, \omega) = \frac{2\tilde{g}(\omega)}{1 - \tilde{g}(\omega)} C_b(z = L, \omega). \quad (69)$$

The resolution of this set of equations is straightforward. Using the fact that $\ell_s \ll L$, an approximate solution is given by

$$C_d(z, \omega) = \left[-2 \frac{g(\omega)}{1 - g(\omega)} + 3 \left\{ 1 + \frac{z_0(\omega)}{\ell_s(\omega)} \right\} \right] I_0 \frac{\sinh[\kappa(\omega)(L - z)]}{\sinh[\kappa(\omega)L]} = 5I_0 \frac{\sinh[\kappa(\omega)(L - z)]}{\sinh[\kappa(\omega)L]}. \quad (70)$$

Thus, close to the output interface in transmission, the normalized correlation is given by

$$C_d(z = L, \omega) = \frac{\kappa(\omega)L}{\sinh[\kappa(\omega)L]} \quad (71)$$

where

$$\kappa(\omega) = \sqrt{\frac{3}{\tilde{\ell}^*(\omega)\tilde{\ell}_a(\omega)}}. \quad (72)$$

Equation (71) is the standard expression we usually obtain in the case of a large absorbing scattering medium except that the usual absorption term describes a decorrelation process here.

B. Second harmonic regime

We now move to the second harmonic regime and we have to apply the standard diffusion equation derivation to the non-linear RTE given by Eq. (45). Since the goal of this section is to obtain analytical results, we have first to make an assumption on the specific intensity at frequency ω that enters the source term in the non-linear RTE. Deeply inside the medium, we consider that its diffuse part is isotropic which gives

$$\tilde{I}(\mathbf{r}, \mathbf{u}, \omega) = C_b(z, \omega)\delta(\mathbf{u} - \mathbf{e}_z) + \frac{C_d(z, \omega)}{4\pi}. \quad (73)$$

The correlation at 2ω is still given by

$$C(\mathbf{r}, 2\omega) = \langle E(\mathbf{r}, 2\omega) \rangle \langle \tilde{E}^*(\mathbf{r}, 2\omega) \rangle + \langle \delta E(\mathbf{r}, 2\omega) \delta \tilde{E}^*(\mathbf{r}, 2\omega) \rangle = C_b(\mathbf{r}, 2\omega) + C_d(\mathbf{r}, 2\omega). \quad (74)$$

The ballistic component can be fully neglected. Indeed, it corresponds to a diagram where both SHG processes for the field and its conjugate take place on statistically independent positions. This implies that phase matching cannot be obtained and this term vanishes. Besides, it is important to note that this diagram is not taken into account in Eq. (45). In order to obtain a diffusion equation for the diffuse component, we first define the first and second moments of the SHG phase function by

$$m_0(z, \omega) = \int S(z, \mathbf{u}, \omega) d\mathbf{u}, \quad m_1(z, \omega) = \int S(z, \mathbf{u}, \omega) \mathbf{u} \cdot \mathbf{e}_z d\mathbf{u} \quad (75)$$

where S is the source term of the RTE at 2ω given by

$$S(z, \mathbf{u}, \omega) = \alpha \iint p_{\text{SHG}}(\mathbf{u}, \mathbf{u}', \mathbf{u}'', \omega) g_{\text{SHG}}(\mathbf{u}, \mathbf{u}', \mathbf{u}'', \omega) \tilde{I}(\mathbf{r}, \mathbf{u}', \omega) \tilde{I}(\mathbf{r}, \mathbf{u}'', \omega) d\mathbf{u}' d\mathbf{u}''. \quad (76)$$

Then, we obtain the diffusion equation for the diffuse component given by

$$\left[-\frac{\tilde{\ell}_s(2\omega)\tilde{\ell}_t(2\omega)}{3} \frac{\partial^2}{\partial z^2} + \frac{\tilde{\ell}_s(2\omega)}{\tilde{\ell}_a(2\omega)} \right] C_d(z, 2\omega) = \tilde{\ell}_s(2\omega)m_0(z, \omega) - \tilde{\ell}_s(2\omega)\tilde{\ell}_t(2\omega) \frac{\partial}{\partial z} m_1(z, \omega) \quad (77)$$

with the boundary conditions

$$C_d(z=0, 2\omega) - \tilde{z}_0(2\omega) \frac{\partial C_d}{\partial z}(z=0, 2\omega) = -\frac{2\tilde{\ell}_s(2\omega)m_1(z=0, \omega)}{1 - \tilde{g}(2\omega)}, \quad (78)$$

$$C_d(z=L, 2\omega) + \tilde{z}_0(2\omega) \frac{\partial C_d}{\partial z}(z=L, 2\omega) = \frac{2\tilde{\ell}_s(2\omega)m_1(z=L, \omega)}{1 - \tilde{g}(2\omega)}. \quad (79)$$

Writing S is the form

$$S(z, \mathbf{u}, \omega) = \alpha C_b(z, \omega)^2 \mathcal{A}(\mathbf{u}, \omega) + \frac{\alpha}{4\pi} C_b(z, \omega) C_d(z, \omega) \mathcal{B}(\mathbf{u}, \omega) + \frac{\alpha}{16\pi^2} C_d(z, \omega)^2 \mathcal{C}(\mathbf{u}, \omega) \quad (80)$$

where

$$\mathcal{A}(\mathbf{u}, \omega) = p_{\text{SHG}}(\mathbf{u}, \mathbf{e}_z, \mathbf{e}_z, \omega) g_{\text{SHG}}(\mathbf{u}, \mathbf{e}_z, \mathbf{e}_z, \omega), \quad (81)$$

$$\mathcal{B}(\mathbf{u}, \omega) = \frac{1}{4\pi} \int p_{\text{SHG}}(\mathbf{u}, \mathbf{u}', \mathbf{e}_z, \omega) g_{\text{SHG}}(\mathbf{u}, \mathbf{u}', \mathbf{e}_z, \omega) + p_{\text{SHG}}(\mathbf{u}, \mathbf{e}_z, \mathbf{u}', \omega) g_{\text{SHG}}(\mathbf{u}, \mathbf{e}_z, \mathbf{u}', \omega) d\mathbf{u}' \quad (82)$$

$$\text{and } \mathcal{C}(\mathbf{u}, \omega) = \frac{1}{16\pi^2} \iint p_{\text{SHG}}(\mathbf{u}, \mathbf{u}', \mathbf{u}'', \omega) g_{\text{SHG}}(\mathbf{u}, \mathbf{u}', \mathbf{u}'', \omega) d\mathbf{u}' d\mathbf{u}'', \quad (83)$$

we get

$$m_0(z, \omega) = \alpha \left[C_b(z, \omega)^2 \mathcal{A}_0(\omega) + \frac{1}{4\pi} C_b(z, \omega) C_d(z, \omega) \mathcal{B}_0(\omega) + \frac{1}{16\pi^2} C_d(z, \omega)^2 C_0(\omega) \right] \quad (84)$$

$$\text{and } m_1(z, \omega) = \alpha \left[C_b(z, \omega)^2 \mathcal{A}_1(\omega) + \frac{1}{4\pi} C_b(z, \omega) C_d(z, \omega) \mathcal{B}_1(\omega) + \frac{1}{16\pi^2} C_d(z, \omega)^2 C_1(\omega) \right] \quad (85)$$

with

$$\mathcal{X}_0(\omega) = \int \mathcal{X}(\mathbf{u}, \omega) d\mathbf{u}, \quad \mathcal{X}_1(\omega) = \int \mathcal{X}(\mathbf{u}, \omega) \mathbf{u} \cdot \mathbf{e}_z d\mathbf{u}, \quad (86)$$

where $\mathcal{X} = \mathcal{A}, \mathcal{B}, \mathcal{C}$. Since we consider that the diffusive regime is valid, we neglect in the following the ballistic component C_b . Thus $\mathcal{A} \sim 0$ and $\mathcal{B} \sim 0$. Moreover \mathcal{C} is of the form

$$\mathcal{C}(\mathbf{u}, \omega) = \frac{1}{16\pi^2} \iint F(6 - 4\mathbf{u} \cdot \mathbf{u}' - 4\mathbf{u} \cdot \mathbf{u}'' + 2\mathbf{u}' \cdot \mathbf{u}'', \omega) d\mathbf{u}' d\mathbf{u}'' \quad (87)$$

which implies that \mathcal{C} is independent of \mathbf{u} . This leads to $C_1 = 0$. Finally, only C_0 is non-zero. In order to have its expression, we note that

$$C_d(z, \omega)^2 = \frac{25I_0^2}{2 \sinh[\kappa(\omega)L]^2} \left[e^{2\kappa(\omega)(L-z)} + e^{-2\kappa(\omega)(L-z)} - 2 \right]. \quad (88)$$

Thus the diffusion equation becomes

$$\left[-\frac{\tilde{\ell}_s(2\omega)\tilde{\ell}_t(2\omega)}{3} \frac{\partial^2}{\partial z^2} + \frac{\tilde{\ell}_s(2\omega)}{\tilde{\ell}_a(2\omega)} \right] C_d(z, 2\omega) = \frac{25I_0\tilde{\ell}_s(2\omega)\alpha C_0(\omega)}{32\pi^2 \sinh[\kappa(\omega)L]^2} \left[e^{2\kappa(\omega)(L-z)} + e^{-2\kappa(\omega)(L-z)} - 2 \right] \quad (89)$$

with the boundary conditions

$$C_d(z=0, 2\omega) - \tilde{z}_0(2\omega) \frac{\partial C_d}{\partial z}(z=0, 2\omega) = 0, \quad (90)$$

$$C_d(z=L, 2\omega) + \tilde{z}_0(2\omega) \frac{\partial C_d}{\partial z}(z=L, 2\omega) = 0. \quad (91)$$

The resolution of this set of equations is still straightforward and we get

$$C_d(z=L, 2\omega) = \frac{6\mathcal{D}(\omega)}{\kappa(2\omega)L \sinh[\kappa(\omega)L]^2 \sinh[\kappa(2\omega)L]} \frac{\kappa(2\omega)^2 \{1 - \cosh[2\kappa(\omega)L]\} - 4\kappa(\omega)^2 \{1 - \cosh[\kappa(2\omega)L]\}}{\kappa(2\omega)^2 - 4\kappa(\omega)^2} \quad (92)$$

where

$$\mathcal{D}(\omega) = \frac{\int p_{\text{SHG}}(\mathbf{u}, \mathbf{u}', \mathbf{u}'', \omega) g_{\text{SHG}}(\mathbf{u}, \mathbf{u}', \mathbf{u}'', \omega) d\mathbf{u} d\mathbf{u}' d\mathbf{u}''}{\int p_{\text{SHG}}(\mathbf{u}, \mathbf{u}', \mathbf{u}'', \omega) d\mathbf{u} d\mathbf{u}' d\mathbf{u}''}. \quad (93)$$

In this expression, we have defined

$$\kappa(2\omega) = \sqrt{\frac{3}{\tilde{\ell}_t(2\omega)\tilde{\ell}_a(2\omega)}}. \quad (94)$$

In the particular case where $\kappa(2\omega) = 2\kappa(\omega)$, we obtain

$$C_d(z=L, 2\omega) = \frac{3\mathcal{D}(\omega)}{\sinh[\kappa(\omega)L]} \left[\frac{1}{\sinh[\kappa(\omega)L]} - \frac{1}{\kappa(\omega)L \cosh[\kappa(\omega)L]} \right]. \quad (95)$$

C. Comparison to Monte Carlo simulations

In order to check the validity of Eqs. (71) and (92), we have performed Monte Carlo simulations in the particular case of a constant displacement amplitude d such that $k_0 d \ll 1$ and $f(\Delta) = \delta(\Delta - d)$. This gives

$$\kappa(\omega)L = b(\omega)k_0 d, \quad \kappa(2\omega)L = 2b(2\omega)k_0 d \quad (96)$$

$$\text{and } \mathcal{D}(\omega) = \frac{1}{8\pi} \int_{\phi=0}^{2\pi} \int_{\mu=-1}^1 \int_{\mu'=-1}^1 \text{sinc} \left[k_0 d \sqrt{6 - 4\mu - 4\mu' + 2\mu\mu' + 2\sqrt{1-\mu^2}\sqrt{1-\mu'^2} \cos \phi} \right] d\mu d\mu' d\phi. \quad (97)$$

An example of the results obtained is reported in Fig. 6 for $b(\omega) = b(2\omega) = 40$, $g(\omega) = 0.31$ and $g(2\omega) = 0.75$. The disorder correlation is given by $k_0 \ell = 1$. A good agreement is obtained.

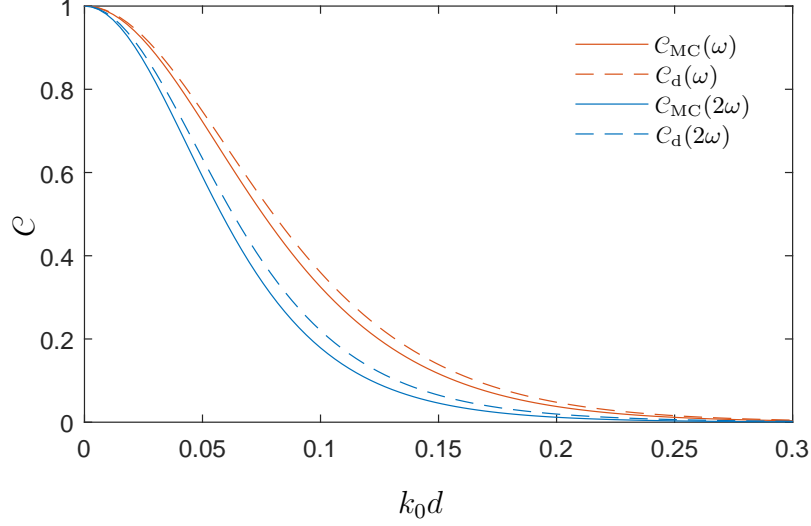


FIG. 6. Comparison of the correlation functions obtained using the Monte Carlo scheme (C_{MC}) and diffusion approximation (C_d) for the linear (ω) and second harmonic (2ω) beams as a function of the normalized displacement distance $k_0 d$. The parameters are $b(\omega) = b(2\omega) = 40$, $g(\omega) = 0.31$, $g(2\omega) = 0.75$ and $k_0 \ell = 1$. $N_p = 28 \times 10^6$ random walk packets are used for the Monte Carlo schemes.

-
- [1] S. M. Rytov, Y. A. Kravtsov, and V. I. Tatarskii, *Principles of Statistical Radiophysics*, Vol. 4 (Springer-Verlag, Berlin, 1989).
 - [2] L. A. Apresyan and Y. A. Kravtsov, *Radiation Transfer: Statistical and Wave Aspects* (Gordon and Breach Publishers, Amsterdam, 1996).
 - [3] M. C. W. van Rossum and T. M. Nieuwenhuizen, Multiple scattering of classical waves: microscopy, mesoscopy and diffusion, *Rev. Mod. Phys.* **71**, 313 (1999).
 - [4] R. Pierrat, Transport equation for the time correlation function of scattered field in dynamic turbid media, *J. Opt. Soc. Am. A* **25**, 2840 (2008).
 - [5] R. Pierrat, R. Carminati, and J.-L. Le Gouët, Photon echoes in strongly scattering media: A diagrammatic approach, *Phys. Rev. A* **97**, 063816 (2018).
 - [6] A. Ishimaru, *Wave Propagation and Scattering in Random Media* (IEEE Press, Oxford, 1997).